Motor cortex somatostatin interneurons adaptively shape the structure of motor sequences

Jeong Oen Lee[1], Sebastiano Bariselli[1,2], Giacomo Sitzia[1,3], and David M. Lovinger[1+]

1. Laboratory for Integrative Neuroscience (LIN), National Institute on Alcohol Abuse and Alcoholism, Bethesda, MD, USA
2. Current address: IRCCS Humanitas Research Hospital, via Manzoni 56, 20089 Rozzano, Milan, Italy
3. Current address: Department of Neuroscience, Københavns Universitet, København, Hovedstaden, Denmark

+Lead corresponding author: David M. Lovinger, lovindav@willco.niaaa.nih.gov

HIGHLIGHTS

- Activation of somatostatin (SST) interneurons in the primary motor cortex (M1) correlates with learning new motor actions and execution of complex motor programs.
- Activity of M1 SST interneurons adapts in response to structural patterns of the motor tasks.
- Inhibition of SST interneuron activity leads to inefficient execution of complex motor programs.

ABSTRACT

The brain can flexibly reorganize motor sequence, or program, execution to efficiently reach positive outcomes. These behavioral adaptations are primarily driven by reinforcement learning, leading to structural and kinematic modifications of consolidated motor programs. While previous studies established the critical contribution of cortical and basal ganglia circuits in controlling motor sequences or movement-by-movement kinematics, the neural mechanisms that adaptively shape efficient motor programs are not fully understood. Here, we found increased action-locked activity and network synchrony of somatostatin (SST) interneurons in the primary motor cortex (M1), compared to desynchronized pyramidal (PYR) neuron calcium activity, upon the acquisition of a single lever-press task in freely moving mice. After motor consolidation, cortical SST interneurons disengaged from action execution and then re-engaged when mice reorganized their motor programs upon changes in task complexity. Notably, the activity of M1 SST interneurons encoded structural and kinematic information of these more complex motor sequences. Finally, we showed that inhibition of SST interneurons interfered with the kinematics and disrupted the efficiency of motor program execution. These findings demonstrate a causal role for M1 SST interneuron re-engagement in regulating efficient motor sequence reorganization.

INTRODUCTION

Humans and other animals can adaptively reorganize the execution of motor sequences (or programs) in response to changes in behavioral contexts and task complexity [1] [2] [3]. This motor refinement process exhibits remarkable similarities across species as animals progressively consolidate and adapt reinforced motor programs [4] [5] [6]. Recent studies suggested two main models recounting the roles of basal ganglia and cortical circuits in motor skill learning and action sequence control. One view highlights that motor regions of the neocortex encode essential parameters of action execution, even when a motor skill is consolidated [7] [8] [9-11]. In contrast, the "cortical disengagement" model posits that cortical regions are essential for the acquisition of new skills [12] but that, once they are learned, basal ganglia circuits primarily oversee motor program execution [13] [14] [15]. Thus, it remains unclear whether basal ganglia circuits would be solely responsible for the adaptation of consolidated motor programs or whether cortical activity "re-engagement" occurs to facilitate motor sequence reorganization.

Pyramidal (PYR) neurons and inhibitory interneurons (INs) in the primary motor cortex (M1) represent action learning and execution through complex and plastic activity patterns tuned to specific movement-related parameters [16-20]. Notably, PYR neurons in M1 layer 5/6 (L5/6) are specialized to relay commands to downstream motor regions, such as brainstem, spinal cord [21], and striatum [9], through pathway-specific subpopulations that independently encode movement direction and amplitude [10]. In parallel, M1 layer 2/3 (L2/3) neurons refine their activity during associative learning [22], encoding both the sensory and motor components of the task as learning progresses [17]. Thus, upper layer M1 neurons might coordinate sensorimotor representations, while deep layer neurons appear embedded in a neural network representing well-learned movements [11]. In the motor cortex, this movement-related cortical activity is often observed as oscillatory patterns [23] or represented by spatiotemporal sequential activation patterns [16], while activity of M1 PYR neurons can even become independent of movement upon extended training [12]. While extensive studies on the motor cortex established that activity of M1 PYR neurons changes based on individual movements, motor tasks, and learning status, little is known about how local inhibitory neurons in M1 contribute to these processes, particularly encoding the acquisition, execution and adaptations of reinforced motor programs.

GABAergic interneurons participate in cortical network computations and gate information flow through the neocortex [24, 25], thus effectively regulating motor program acquisition and execution. Vasoactive intestinal peptide (VIP)- and somatostatin (SST)-positive INs mediate the integration of extra-cortical sensory information within the M1 [26], while parvalbumin (PV)- and SST INs actively regulate neighboring PYR neuronal activity at movement onset in a task-specific manners. [18, 19 , 20, 27, 28]. Layer 2/3 (L2/3) somatostatin (SST) and parvalbumin (PV)-positive INs determine synaptic and structural plasticity of PYR neurons, thus effectively enabling motor skill acquisition [29]. Additionally, the activity of SST INs in L2/3 of M1 exhibits task-specific regulation, which is associated with the retention of previously learned motor skills [27, 28]. Thus, it has been

suggested that cortical IN activity may exert critical regulation during context-dependent motor control and motor skill encoding [30]. However, how cortical INs specifically contribute to the execution and adaptation of re-organized motor programs remains unclear.

In this study, we monitored single-cell calcium activity of PYR and SST INs in M1 L5/6 while freely moving mice progressively reorganized reinforced action programs from a single lever-press (fixed ratio 1, FR1) to a time-constrained FR4 sequence of lever-presses. We found that SST INs in layer 5/6 exhibited action-specific calcium activity in a single lever-press task. To test whether SST INs activity continuously correlated with the action or, instead, aligned with the cortical "disengagement" model, we extended the FR1 training and found that calcium activity and network synchrony of L5/6 SST INs decreased with task consolidation. In contrast, during time-constrained FR4 training, as motor sequences became more complex, the activity of SST INs increased while dynamically encoding the kinematics of motor sequences. Chemogenetic and optogenetic inactivation of SST INs interfered with motor sequence kinematics and impaired efficient motor program execution. Consequently, these results support the idea of cortical IN "re-engagement" during the execution of complex motor programs.

RESULTS

Action-Locked Activation of M1 SST Network Upon Motor Program Acquisition

To examine the activity of identified cortical neuron subtypes during motor program acquisition, we trained mice in a self-paced lever-press task (**Fig.1a**). We monitored *in vivo* single-cell calcium activity in the M1 with a miniaturized fluorescence microscope and implantable gradient-index (GRIN) lenses. After viral transduction of the genetically-encoded calcium indicator GCaMP6f, we assessed calcium transients in PYR neurons and SST INs across distinct groups of mice while animals performed a fixed-ratio one (FR1) lever-pressing task (**Fig.1a**). From Day 1 (D1, early) to Day 7 (D7, late) of training, animals displayed a dramatic increase in lever-press rate (**Fig. 1b**), indicating the acquisition of the novel motor task. On D7, SST INs in M1 exhibited action-locked calcium activation and synchronized population activity (**Fig.1c**). During a training session, calcium traces ($\Delta F/F_0$ in %, where F_0 indicates fluorescence baseline) of individual SST INs exhibited less complex patterns than calcium traces from PYR neurons (**Extended Fig.1 a,b**). These calcium traces were reconstructed into peak-normalized activity maps (**Extended Fig.1c, d**) to identify the timing of peak calcium increases relative to lever press. Consistent with previous studies in head-fixed mice [27] [16], the activity pattern of PYR neurons revealed a sequential action-locked activation pattern (**Extended Fig. 1c**), which resulted in a distributed calcium event probability (**Extended Fig.1e**). In contrast, SST INs displayed calcium event probabilities that were highest around lever-presses (**Extended Fig.1f**). We then characterized the layer-specificity of action-locked calcium traces ($\Delta F/F_0$ in %) in PYR neurons and SST INs by adjusting the depth of GRIN lens implants and recording neurons in L2/3 and L5/6 of the M1 (**Extended Fig.1g,h,i**). As expected,

population average of PYR calcium traces in L2/3 and L5/6 exhibit minimal transient amplitude time-locked to the lever press (**Extended Fig. 1h**). Notably, while SST INs of L2/3 showed small transient amplitude, SST INs in L5/6 exhibited pronounced transient amplitude in the population average of calcium traces around lever-presses (**Extended Fig.1i**). Further analysis of the calcium responses of individual neurons revealed that SST IN activity in M1 L2/3 exhibited variability in both calcium traces (**Extended Fig.1j**) and the corresponding peak normalized activity map (**Extended Fig.1k,l**). The same analysis showed that SST INs in L5/6 displayed consistent action-locked calcium responses (**Extended Fig. 1m,n,o**). We then assessed M1 SST network synchrony as Pearson's cell-to-cell correlation coefficient. This parameter calculates the linear relationship between a single cell calcium trace and all other neuronal traces during a 10 second time window centered around the lever-press. The analysis revealed that network synchrony was higher in SST than PYR network in L5/6, but not in L2/3 (**Extended Fig.1p**). Thus, we further investigated how the heightened SST IN calcium activity in M1 L5/6 changes during motor program consolidation and motor sequence reorganization.

Disengagement of Action-locked M1 SST Network Activity Upon Motor Program Consolidation

To understand whether action-locked SST activity would change upon motor program consolidation, we compared neuronal population activity between early (day 7, D7) and extended (day 21, D21) FR1 training in the same experimental subjects (**Fig.1 c,d**). In M1 L5/6 SST INs, we observed decreased action-locked fluorescence responses at D21 compared to D7 (**Fig.1e-h**). To determine if this decrease was caused by long-term fluorescence degradation, we additionally assessed the maximum $\Delta F/F_0$ peaks and action-locked $\Delta F/F_0$ responses across training sessions normalized to D1. While the maximum $\Delta F/F_0$ response normalized to D1 did not change across training sessions (**Extended Fig.1q,r**), the normalized action-locked $\Delta F/F_0$ responses decreased over training sessions (**Extended Fig.1s)** and were smaller at D21 compared to D7 (**Extended Fig.1t)**. In these experimental settings, long-term imaging and training did not decrease the overall amplitude of calcium transients, but rather result in the reduction of action-locked SST IN activation.

By detecting peak locations of $\Delta F/F_0$ responses, we also analyzed discrete calcium events (**Fig.1i,j**) from individual SST INs. At a single-cell level, action-locked calcium event frequency decreased from D7 to D21 (**Fig1.k-n**), with no changes in the temporal distribution of event probability (**Fig.1o,p**). We also observed a significant decrease in Pearson cell-to-cell correlation coefficients of SST activity across subsequent lever presses at D21 compared to D7 (**Fig.1q,r**). Thus, SST IN activity exhibited a progressive decrease in action-locked synchrony, which overlapped with SST disengagement from action execution upon long-term training.

Action-locked Re-engagement of M1 SST Network Upon Motor Program Reorganization

Because of the decreased action-locked SST IN activity during simple motor program consolidation, we directly tested the "re-engagement" hypothesis by examining cortical SST network dynamics while animals

reorganized simple actions into complex motor sequences. First, we trained animals for seven days on an FR1 schedule followed by seven days of non-time-constrained FR4 (NTC-FR4) training [31] to allow for the acquisition and consolidation of baseline motor programs (**Extended Fig.2a,b**). Next, we trained mice to progressively increase their lever-press rate and eventually construct a sequence of 4 or more consecutive lever presses within progressively shorter time limits (4, 2, and 1 sec) to obtain a reward. This time-constrained schedule (TC-FR4) increased lever-press frequency across sessions (**Fig.2a**). We then analyzed kinematic parameters within a unit sequence (SEQ), which we defined as a sequence of consecutive lever presses followed by either a head entry or a pause longer than 3 seconds (**Fig 2b**). In addition to the overall increase in lever press rate, the TC-FR4 training schedule led mice to increase the frequency (**Fig.2c**) and the number (**Fig.2d**) of lever presses within a SEQ compared to the last session of NTC-FR4. This indicates alterations in SEQ structure that were not observed across NTC-FR4 training (**Extended Fig.2c,d**). To simplify the representation of SEQ kinematic parameters, we defined the sequence efficiency (SEQ efficiency, **Fig.2e**) as a function of lever-press rate and number of lever presses in a SEQ. As such, efficient SEQs (e.g., fast-quadruple lever presses at >4Hz) were always followed by reward delivery and projected into a bright region on the color-coded map (**Fig.2e**). In contrast, inefficient SEQs (e.g., slow-and-many lever presses or fast-and-few lever presses) have low SEQ efficiency coefficients and fall in the darker regions of the colormap. As mice learned to perform 4Hz-TC-FR4 SEQs, the SEQ efficiency increased compared to NTC-FR4 training sessions (**Fig.2f**), indicating successful motor sequence reorganization. Concurrent with motor program reorganization, the action-locked single-cell or population fluorescence responses of SST INs increased at 4Hz-TC-FR4 compared to NTC-FR4 (**Fig.2g-l**). Note that when the SEQ efficiency remained unchanged during the NTC-FR4-training (**Extended Fig.2e,f**), there was a reduction in the population fluorescence response (**Extended Fig.2g-j**), which indicated SST IN disengagement. These data demonstrate that calcium activity of SST INs display a task-dependent and action-locked bidirectional modulation.

We further examined the distribution characteristics of calcium events of SST INs. In the 4Hz-TC-FR4 schedule, the frequency of action-locked calcium events increased compared to the NTC-FR4 schedule (**Fig.2m-r**). Also, the action-locked calcium event probability during the 4Hz-TC-FR4 training schedule was temporally delayed (**Fig.2s,t**) compared to the NTC-FR4 schedule. Importantly, we did not detect differences in Pearson correlation coefficient of SST single-cell activities between 4Hz-TC-FR4 and NTC-FR4 training sessions (**Fig.2u,v**). This indicates the maintenance of SST IN synchrony as mice efficiently reorganized their behavior from simple to more complex motor programs. Altogether, these data demonstrate the re-engagement of SST INs during execution and reorganization of complex motor programs.

SST Network Activity Encodes Kinematics and Structural Classes of Complex Motor Sequences

The observation of an increased calcium response and maintained SST network synchrony suggest that SST IN re-engagement might encode kinematic information related to complex motor program execution. Thus,

175 it became critical to examine whether distinct calcium activity profiles were associated with the structural aspects
176 of the motor sequence even within the same training session. To examine this, we first performed a correlation
177 analysis between SEQ efficiency and the corresponding amplitude of calcium response for all SEQs within the
178 4Hz-TC-FR4 training session. We observed a positive correlation between these parameters (**Fig.3a**),
179 suggesting that larger calcium transients underlie more efficient SEQs.

180 To directly compare calcium transients between SEQs with different kinematic structures, we performed
181 unsupervised hierarchical clustering of SEQs within a 4Hz-FR4 training session (**Fig3.b**). The analysis revealed
182 three distinct SEQ sub-classes; Class1 (C1), which are the most represented (46.0% of all SEQs) at this training
183 stage, consists of SEQs with an action-tight lever-press distribution and rapid lever-press rates (**Fig.3c**). Class
184 2 (C2, 29.5%) contains SEQs with a less confined lever-press distribution and slower lever-press frequency,
185 while Class 3 (C3,24.5%) comprises SEQs with numerous lever-press and slower lever-press rates (**Fig.3c**).
186 Thus, we reorganized the fluorescence profiles and behavioral data according to this classification. C3 SEQs
187 showed a higher number of presses per SEQ relative to C1 and C2 (**Fig.3d**). In contrast, C1 showed the highest
188 frequency within a SEQ (**Fig.3e**). Thus, motor sequences in C1, C2, and C3 were also separately clustered on
189 the SEQ efficiency map (**Fig.3f**). When we compared fluorescent transients of SST INs across different SEQ
190 classes within the same training session, we observed that the most efficient C1 SEQs had higher peak
191 amplitudes compared to Class 2 and 3 SEQs (**Fig. 3g**).

192 To characterize the calcium transients underlying the most efficient SEQs that led to reward retrieval, we
193 further defined a subset of C1 SEQs as “complete SEQ” when they contained fast/confined (>4Hz) consecutive
194 lever presses and were followed by reward retrieval (**Fig.3h,i**). In contrast, a subset of C3 SEQs were defined
195 as “incomplete SEQ” when mice executed slow and elongated lever press sequences without reward retrieval
196 (**Fig.3j**). Less than half of C3 SEQs fall in the “incomplete” category (**Fig.3h**). Incomplete SEQs contained a
197 higher lever-press number (**Fig.3k**) and had a lower lever-press frequency (**Fig.3l**) compared to complete SEQs.
198 As a result, complete and incomplete SEQs have high and low SEQ efficiency coefficient, respectively (**Fig.3m**).
199 Importantly, distinctive neural responses are associated with the execution of these two SEQ subclasses.
200 Calcium transients during complete SEQs had significantly larger peak amplitude than those associated with
201 incomplete SEQs and persisted for a few seconds after action initiation (**Fig.3n,o**). Notably, plotting the
202 relationship of the amplitude of SST IN calcium responses and SEQ efficiency segregated the complete and
203 incomplete SEQs (**Fig.3p**). Altogether, different kinematics and structural classes of SEQs were distinctively
204 encoded in SST INs activity. Specifically, SST IN activity was higher during efficient SEQs that were appropriately
205 structured and led to successful reward retrieval.

206

207

208 **Negative Modulation of SST IN Function Impairs Motor Sequence Kinematics**

209 Considering our observation of a strong association between SST IN re-engagement and efficient motor
210 execution, we hypothesized that inhibition of SST INs would interfere with efficient lever pressing during motor
211 program re-organization. We tested this idea using chemogenetic modulation with the Gi-coupled hM4Di
212 Designer Receptor Exclusively Activated by Designed Drug (DREADD) designed to interfere with SST IN activity.
213 In hM4Di expressing M1 interneurons (**Extended Fig. 4a, b**), we measured resting membrane potential and
214 observed that hM4Di expression in SST-Cre mice induced neuronal hyperpolarization upon CNO bath
215 application *ex vivo* (**Extended Fig.4c**). Next, we analyzed lever-pressing behavior in control (SST Cre-negative)
216 and hM4Di-DREADD expressing mice (SST Cre-positive) during the TC-FR4 training schedule (**Fig.4a**).
217 Intraperitoneal injection of Clozapine-N-oxide (CNO, 5mg/kg) increased the average lever-press rate (**Fig. 4b**)
218 in the SST Cre-positive, but not Cre-negative mice, particularly during the most time-constrained training
219 schedules (i.e. 4 and 8 Hz). We found that this increase was due to increased lever press numbers within a SEQ
220 in hM4Di-expressing mice compared to the control group across training days (**Fig.4c**). This effect also reduced
221 SEQ efficiency in hM4Di-expressing mice compared to control animals (**Fig.4d**). These data suggest that,
222 despite an overall increase in lever press rate, chemogenetic-mediated hyperpolarization of M1 SST
223 interneurons deteriorates sequence organization. To further investigate this point, we analyzed lever-press
224 distribution within each SEQ. While control mice injected with CNO displayed a temporally confined lever-press
225 distribution around sequence initiation, hM4Di-CNO inhibition led to prolonged lever pressing (**Fig. 4e**). In fact,
226 the normalized lever-press probability distribution after sequence initiation was elongated in hM4Di-expressing
227 animals compared to controls (**Fig.4f**). Disruption of efficient lever pressing in hM4Di-expressing mice was also
228 highlighted by an increased and decreased proportion of "incomplete" (**Fig.4g**) and "complete" sequences
229 (**Fig.4h**), respectively. These data demonstrate a direct contribution of M1 SST interneuron re-engagement in
230 the organization and execution of efficient motor sequences.

231

232 **Action-locked Inhibition of SST INs Disrupts Efficient Motor Sequences**

233 Our chemogenetic results demonstrate that negative modulation of SST INs disrupts the kinematic
234 structure of complex motor programs during a period of re-engagement of the activity of these neurons. However,
235 the DREADD approach interfered with SST interneuron function throughout the duration of each training session,
236 perhaps leading to long-lasting effects on basal SST activity and broader cortical networks on a minute-to-hour
237 timescale. To avoid these confounding effects, we aimed to silence action-locked neuronal activity through
238 closed-loop optogenetics during SST IN re-engagement. To do so, we expressed either the inhibitory opsin
239 (eNpHR) or control fluorescence protein (eYFP) in M1 SST INs using SST-Cre mice. We delivered laser light
240 (wavelength: 532nm, intensity: ~4mW) during TC-FR4 training sessions (**Fig.5a**). Within these sessions, each
241 action initiation (first lever press) triggered a continuous five sec-long laser illumination (**Fig. 5a**) to inhibit
242 sequence-related neuronal activation that persists typically for several seconds as the lever press sequence

243 continues. Laser illumination in eNpHR-expressing mice led to an increase in average lever-press rate (**Fig. 5b**)
244 and the number of lever presses within a SEQ (**Fig.5c**) compared to eYFP animals, particularly during the most
245 time-constrained training schedules (4 and 8Hz). Similar to the results obtained with chemogenetic negative
246 modulation, the SEQ efficiency decreased in eNpHR compared to eYFP-expressing mice (**Fig.5d**). Additionally,
247 SST optogenetic silencing elongated the lever-press probability distribution at action initiation (**Fig. 5e and f**),
248 increased the proportions of incomplete sequences and decreased the percentage of complete sequences (**Fig.**
249 **5g and h**) compared to controls.

250 Next, we investigated whether optogenetic silencing of SST IN activity would directly modulate kinematic
251 structure of motor sequences within a single experimental subject. This was accomplished by alternating laser-
252 ON and laser-OFF periods and assessing the corresponding lever-press SEQs (**Fig. 5i**). In our Periodic Laser
253 Modulation (PLM) protocol, the action-specific laser-illumination was alternatively enabled and disabled every
254 five-minutes (**Extended Fig.5a**). When the optogenetic inactivation onto SST INs was disabled (laser-OFF
255 periods), the eNpHR group demonstrated lower lever-press rate (**Fig. 5j**) and number of lever presses within a
256 sequence (**Fig. 5k**), compared to laser ON periods within the same training session. This modulation was not
257 observed in the eYPF group (**Fig.5j,k**). Next, we assessed the distribution profile of lever-press probability as a
258 function of laser modulation. In the eNpHR group, we found that the elongated lever-press probability distribution
259 observed during the laser-ON periods was reorganized into a more efficient lever-press distribution when the
260 optogenetic SST silencing was deactivated (**Extended Fig.5b**). As a result, while the proportion of complete
261 SEQs remained unaffected within the PLM training schedule (**Fig.5m**), the proportion of incomplete SEQs within
262 the eNpHR group during the laser-OFF periods was significantly lower than laser-ON periods (**Fig.5l**). Moreover,
263 the PLM protocol in the eNpHR group decreased SEQ efficiency when the laser-OFF mode changed to laser-
264 ON mode (**Fig.5n**). These results demonstrate that SST IN activity controls the execution of efficient sequence
265 structure in an action-and-time specific manner.

266

267 **DISCUSSION**

268 We investigated single-cell calcium activities in the M1 of freely moving mice as they progressively
269 reorganized reinforced motor programs from a single lever press to a time-constrained sequence of four lever
270 presses. We observed that M1 SST IN activity disengages from lever pressing as action learning and
271 consolidation progresses (**Fig.1**) but re-engages upon changes in motor program execution when the behavioral
272 context complexity increases (**Fig.2**). Moreover, we found that heightened M1 SST IN activity encodes structural
273 and kinematic information on motor sequences, such as the number and frequency of lever presses within a
274 sequence, and correlates with efficient motor program execution (**Fig.3**). Chemogenetic inhibitory modulation
275 and action-locked optogenetic silencing of SST INs decreased motor efficiency, demonstrating a causal link
276 between SST IN re-engagement and execution of complex motor programs (**Fig.4 and 5**).

While it is established that reinforcement learning drives adaptive sequence reorganization, little is known about the neural mechanisms encoding and organizing complex motor sequences. Previous evidence from our laboratory indicates that increased calcium activity of both associative and motor cortex striatal projection neurons is observed during early training. However, as learning progresses, associative inputs to dorsomedial striatum show stronger disengagement compared to the M1-dorsal striatal pathway [9]. These data align with the idea that neural activity in M1 persistently represents action performance and kinematics even after extensive skill learning, although the M1 contribution may undergo some refinement [7] [8, 10, 11]. On the contrary, the "cortical disengagement" model proposes that M1 activity becomes decorrelated from action execution upon consolidation of a given motor program [12, 13]. This model suggests that cortical output is less important for movement control as proficiency is gained. Despite extensive studies in M1 PYR neurons, it is unclear whether and how cortical engagement and disengagement modes are determined within cortical microcircuits. Thalamic input drives the generation of movement-related patterns in M1 [32]. Moreover, M1 local circuits integrate sensory information through inhibitory networks that involve different subtypes of cortical INs (e.g., PV, SST, VIP) [26] [24]. Thus, while neural signals continuously flow into M1 local circuits from other brain regions [33, 34], cortical INs may be crucial in processing and integrating sensory information and regulating neighboring pyramidal neurons[35], effectively shaping outgoing motor commands. M1 SST interneurons have shown task-specific regulation of Ca^{2+} transients within PYR neuronal dendrites [28] and contribution to preserving motor skill execution [27], while facilitating learning-dependent morphological changes in PYR neurons [29]. These results suggested the importance of M1 SST interneurons in regulating PYR neurons during adaptive motor behavior. Our findings of diminished SST IN activity following extended FR1 training (**Fig.1**) are consistent with the "disengagement" model [12, 13]. Concurrently, our observations in the more complex, time-constrained motor sequences also suggest "re-engagement" of cortical activity as task demand increases and proficiency becomes poorer (**Fig.2 and 3**). These results broadens the functional understanding of cortical microcircuits by directly demonstrating that SST IN disengagement and re-engagement shape action reorganization and the efficient execution of reinforced motor programs.

Our study also provides insights into cortico-striatal circuit function during motor program execution. Prior studies primarily focused on modulating SST IN activity to assess its impact on PYR neuron plasticity and dynamics during motor skill learning [27, 29]. However, a direct investigation of SST IN activity during the re-organization of complex motor programs in freely moving mice was lacking. On the other hand, other research focused on establishing a central role for striatal circuits in controlling action sequence initiation, termination, and modulation [15, 31]. In this context, our findings implicate SST INs as fundamental upstream regulators for the efficient execution of complex motor sequences. Thus, in addition to enabling plasticity of PYR neuron dynamics during motor learning [27, 29], action-locked SST IN re-engagement might exert an inhibitory control on deep layer M1 PYR neurons. This further suggests that SST IN might constrain PYR neuron activity to specific action sequence features to "fine-tune" complex motor programs.

Beyond encoding specific features of action sequences, cortical SST IN activity becomes particularly critical during motor program adaptations in response to changes in the behavioral task. In fact, chemogenetic and optogenetic inhibition disrupted motor sequence efficiency specifically during 4Hz and 8Hz TC-FR4 lever-press training, coinciding with the generation of temporally confined lever-pressing structures. Both chemogenetic and optogenetic inhibition led to an increase and a decrease of the percentage of incomplete and complete lever press sequences, respectively (**Fig. 4 and 5**). These data are generally consistent with previous studies showing that optogenetic inhibition of SST INs impaired the acquisition of stereotyped movements in head-fixed mice during a lever-pressing task [29]. Moreover, in other studies monitoring PYR neurons while manipulating SST INs, it was found that SST IN inhibition impairs structured running only when mice have to adapt their behavior from forward- to backward-running on a treadmill task [27]. Our results further extend this perspective on adaptive motor behaviors that SST INs contribute to motor program execution in a task-and-learning dependent manner [30]. In addition to these effects, we also observed that inhibition of SST activity prolonged the temporal distribution of lever press probability, suggesting that SST interneuron activity might also regulate the termination of motor sequences, which is crucial for organizing and reorganizing temporal structure of motor programs [36].

Future investigations will clarify the synaptic and circuit mechanisms underlying SST IN re-engagement and their roles in action initiation and termination during motor program adaptions. These studies characterizing the precise roles of SST IN re-engagement during motor program adaptations will allow preclinical researchers to identify potential SST IN deficits in movement disorders and leverage them as therapeutic targets to restore appropriate action execution [37, 38]

METHODS

Animals

All animal protocols were performed in accordance with the guidelines for care and use of laboratory animals of the US National Institutes of Health approved by the US National Institute on Alcohol Abuse and Alcoholism (NIAAA) Animal Care and Use Committee. Viral injections and implant surgery were performed on 3- to 8-month-old male and female mice. Wild-type C57/Bl6J mice (JAX Stock #: 000664) were purchased from the Jackson Laboratory. Homozygous SST-Cre mice (JAX stock #: 013044; Sst tm2.1(cre)Zjh /J) were crossed with the wild-type C57BL6/J mice (JAX Stock #: 000664) in the NIAAA animal facility. The Cre-positive (SST+) heterozygous offspring were used for imaging and behavioral experiments. Depending on experimental design, we also obtained Cre-positive (SST+) and Cre-negative (SST-) offspring as cage mates from the wild-type C57BL6/J mice (JAX Stock #: 000664) and the heterozygous SST Cre-positive (SST+) mice. When the viral expression was not driven by Cre recombinase, C57/Bl6J mice (JAX Stock #: 000664) were purchased and used in the behavioral experiments.

348

349 **Recombinant adeno-associated viral (AAV) vectors**

350 The following Cre recombinase-dependent adeno-associated viral vectors were used in the calcium
351 imaging, optogenetic, and chemogenetic experiments: AAV1/9 CAG FLEX GCaMP6f (titre $1.9x10^{13}$,
352 Addgene # 100836-AAV1), AAV9.CamKII.GCaMP6s (titre, $2.5x10^{13}$, Addgene# 107790-AAV9), AAV2-
353 hSyn-DIO-hM4D(Gi)-mCherry (titre $1.9x10^{13}$, Addgene# 44362-AAV2), AAV1-Ef1a-DIO-eNpHR 3.0-
354 EYFP (titre $7x10^{12}$, Addgene# 26966-AAV1), AAV1-Ef1a-DIO-eYFP (titre $2.7x10^{12}$, Addgene# 27056-
355 AAV1).

356 **Virus injections**

357 To achieve Cre-dependent expression of genetically encoded fluorescent calcium indicators in SST+
358 cells, AAV vectors containing FLEX-GCaMP6f were micro-injected bilaterally (or unilaterally if noted)
359 into the primary motor cortex (forelimb area [39]) of SST-Cre mice by stereotaxic surgery (AP, anterior-
360 posterior to bregma:0.0~1.0mm, ML, medio-lateral to bregma: +/-1.5mm, DV, dorso-ventral:-0.5mm
361 from the brain surface). For the expression of calcium indicator in pyramidal neurons, AAV vectors
362 containing a CaMKII promotor were injected in C57BL6/J mice. All other viral injections for optogenetic
363 and chemogenetic experiments followed similar microinjection procedures. AAV2-hSyn-DIO-
364 hM4D(Gi)-mCherry,AAV1-Ef1a-DIO eNpHR 3.0-EYFP, and AAV1-Ef1a-DIO EYFP were bilaterally
365 injected depending on the experimental design. First, mice were anesthetized (Isoflurane 1∼2% with
366 respect to oxygen volume) on a secured stereotaxic frame (Kopf Instruments, Germany). After the mice
367 were deeply anesthetized, a longitudinal head skin incision was made to expose the skull. Craniotomies
368 were carried out using a dental drill and the virus solution was microinjected using a 32-gauge syringe
369 (Hamilton,#65458-01) at a volume of 300nL/site with a rate of 50 nL/min. After infusion, the syringe
370 needle was left in place for an additional 5-8 min before removal. Finally, the incisions were closed with
371 VetBond (3M ,1469Sb). The animals were then placed into recovery cages for 3 days with partial
372 heating, and back to home cages for at least 2-3 weeks before secondary chronic implant surgery. In
373 chemogenetic experiments, mice recovered for 5-6 weeks in their home cages without implant
374 surgery.

375 **Imaging lens and fiber implantation**

376 2-3 weeks after the virus injection, craniotomies were performed above the injection site again under
377 Isoflurane anesthesia. The skull surface was cleaned with a diluted hydroperoxide solution. After drilling
378 and enlarging the hole in the skull (1~2mm in diameter) to expose the target brain surface, the dura
379 mater was removed from the surface using gentle aspiration. To image neurons in deep cortical layers
380 (M1 layer 5/6), a 500-µm diameter, 4.0-mm long gradient-index (GRIN) lens (Inscopix,#1050-004417
381 or GoFoton, # CLES050GFT120) was slowly implanted (~0.2 mm/min) until the target depth was
382 reached (DV:-0.5mm from the brain surface). For superficial M1 layer (layer 2/3) imaging, a GRIN lens
383 with a large diameter (1.0mm, Inscopix#1050-004637 or 1.8mm, Edmund #64-519) was placed on top
384 of the brain surface using a stereotaxic frame. If necessary, a lens adaptor was attached after unilateral
385 implantation of the GRIN lens. For optogenetic experiments, fiber ferrules (Thorlabs CFMLC12L02,
386 1.25mm, 0.39NA, L=2mm) were bilaterally implanted (DV:-0.5mm from the brain surface). Once the
387 GRIN lens or fiber ferrules were securely located, cyanoacrylate (Parkell, C&B Metabond, Radiopaque
388 L-Powder, S396) and dental cement (Stoelting, #51459) were applied to fix the optical implant. After
389 the implantation surgery, animals received ketoprofen injections to reduce pain and inflammation for 3
390 days and then recovered in partially heated cages before returning to their home cages. Mice for

391 calcium imaging experiments were singly housed after surgery. Mice expressing eNpHR or eYFP for
392 optogenetic experiments were littermates and group-housed after fiber ferrule implantation.

393 **In-vivo calcium imaging**

394 2-3 weeks after the implantation surgery, the quality of in-vivo fluorescence images and spontaneous
395 fluorescence transients were assessed in home cages and operant boxes without behavioral tasks (no
396 levers, no cues). Before the operant training, this inspection was conducted for a week to validate the
397 stability of the fluorescence images. During this time, the mice were also habituated to carrying a head-
398 mounted microscope device and to handling. After the daily image inspection, the mice underwent
399 additional habituation training (1hour a day), during which they carried a 3D-printed mock device (2.5g)
400 in their home cages. Once it was confirmed that the fluorescence imaging provided stable recordings
401 of spontaneous cellular calcium dynamics, the mice underwent food restriction protocols for operant
402 training. Fluorescence images were collected through three open-source head-mounted microscopes
403 (LABmaker, Miniscope V3.2) and one commercial head-mounted microscope (Inscopix, nVoke
404 System) with a sampling frequency of 10 Hz. Each head-mounted microscope device and specific
405 recording parameters were exclusively assigned to designated animals throughout the duration of the
406 experiments. Synchronized behavior log acquisition and fluorescence image recording were controlled
407 by a digital controller (Med-Associates, MED-PC IV Behavioral Control Software Suite). The raw video
408 images were analyzed using image processing software (NIH ImageJ 1.53, and Inscopix, IDEAS
409 platform) and custom MATLAB scripts.

410 **Calcium image data analysis**

411 The raw fluorescence images were compressed with a 1:4 spatial ratio using image processing
412 software (NIH, ImageJ 1.53 or Inscopix, IDEAS platform) and movement artifacts were corrected
413 (Inscopix, IDEAS platform). The field of view (FOV) was then adjusted and cropped to include images
414 within the GRIN lens. To generate $\Delta F/F_0$ image stacks, the change in fluorescence ($\Delta F = F - F_0$) was
415 calculated for each individual pixel using a custom MATLAB script, where F represents the fluorescence
416 intensity of the pixel, with the baseline F_0 set as the lower envelope of spontaneous fluorescence
417 intensity of individual pixels along the time-axis (analysis code is available online). A CNMF-E algorithm
418 [40] was then employed within the custom MATLAB script to identify the cell locations/features and to
419 extract the single-cell $\Delta F/F_0$ traces. In brief, the CNMF-E algorithm identified the cellular features and
420 their central locations based on pixel-to-pixel signal correlation in the time domain. The custom
421 MATLAB script automatically assigned regions-of-interest (ROIs) around these identified centers of
422 individual cells. Within each ROI, it eliminated rank-1 background fluorescence [40] and crosstalk
423 components from other neurons. The script then recalculated the pixel-to-pixel signal correlation within
424 the ROI and set the boundary of the dominant neuron. The average $\Delta F/F_0$ was computed within the
425 assigned cell boundary. Thus, the $\Delta F/F_0$ in the single cell characteristics (Fig.1 e,f , Extended Fig.1 h,I,
426 and Fig.2 i,j) preserves the same unit representation ($\Delta F/F_0$ in %, where F_0 indicates the spontaneous
427 fluorescence baseline) as in the $\Delta F/F_0$ image stacks. If post-analysis normalization was required for
428 single-cell characterization it is indicated. Following automated trace extraction, identified neurons and
429 their corresponding traces were manually inspected, and any misidentified artifact cells were removed.

430 **Single lever-press (FR1) training**

431 Food restriction started 3 days before any behavioral training. During the entire training period, the
432 body weight of mice was maintained around 85%~90% of their baseline weight by restricting food
433 supply. On the first day in an operant chamber, the mice were trained to retrieve food pellets from the
434 magazine with a random delivery schedule (no cue, no levers). On the following 3 days, the mice were
435 trained on a continuous reinforcement schedule with a fixed ratio (FR1) schedule, where mice earned

436 the reward by making a single lever press. Only one active lever was available. The total number of
437 rewards gradually increased to 5, 15, and 30 in each day. Each daily session ended when the maximum
438 session time of 90 min or the maximum number of rewards set for that session was reached, whichever
439 came first. During this 4-day pre-training, all animals were trained under untethered conditions. Then
440 the following day was designated as Day 1(D1) of the FR1 training while calcium imaging was started.
441 We defined Day 7(D7) as the baseline for the FR1 training, and the FR1 schedule was maintained until
442 Day 21 (D21). In-vivo calcium imaging was performed once or twice a week. On days when the calcium
443 image recording was not performed, mice carried a mock device with a 3-D printed structure identical
444 to the head-mounted microscope (minisciope.org 3D-models or inscopix, dummy microscope#1050-
445 003762) during their daily operant task training. All mice underwent the same daily training protocol
446 and received additional daily food supply (1-3g depending on the daily body weight) after the operant
447 task training in their home cages.

448 **Lever-press sequence (NTC-FR4 and TC-FR4) training**

449 Mice underwent the same food restriction and followed the 4-day pre-training schedule (magazine and
450 FR1 training) and the subsequent 7-day FR1 training schedule described above. After completion of
451 this initial FR1 training, the sequence training schedule began. On the subsequent seven days, all mice
452 were trained on a fixed ratio 4 (FR4) schedule, where the reward was delivered after the 4th lever press
453 without a time-limit. We refer to this FR4 training as non-time-constrained (NTC)-FR4 training to
454 contrast with the following time-constrained (TC)-FR4 training. The following day, the TC-FR4 training
455 was conducted, in which mice were trained to perform organized and sequential lever-presses within
456 specific time criteria to earn a reward. In the first stage of the TC-FR4 training, four consecutive lever-
457 press sequence had to be made within 4 sec (1Hz for 4 lever presses) to earn a reward. The 1Hz
458 schedule was maintained until all mice could achieve 20 complete sequences within 90 min. This
459 training took 2 to 5 days. Next, a 2-second time-limit (2Hz for 4 lever presses) was assigned until all
460 mice in a cohort accomplished 20 complete sequences within a 90 min session. If this training was
461 insufficient, some mice could not earn any reward in the next updated schedules and experienced
462 extinction responses. To complete the 2Hz-TC-FR4 sequence, freely moving mice took 5 days, optics-
463 fiber tethered mice took 7 days and mice carrying the head-mounted microscope took 9 days to meet
464 these criteria. Next, the 1-second (4Hz for 4 lever presses) time-limit was assigned. The calcium
465 imaging experiment stopped on D21 after the first day (D1) of the NTC-FR4 training. Otherwise, the
466 4Hz schedule continued for 5 days in chemogenetic and optogenetic experiments. The final 0.5-second
467 time limit (8Hz for 4 lever presses) was assigned for another 5 days to compare the behavior between
468 control group and experimental group.

469 **Chemogenetic inhibition during sequence lever-press (TC-FR4) training**

470 Operant training was conducted at least 6 weeks after the stereotaxic injection of AAV-DIO-hM4Di-
471 DREADD. The SST-Cre-positive (Cre+) and Cre-negative (Cre-) cagemates were allocated into the
472 hM4Di group and the control group, respectively, and were co-housed during the period of surgical
473 recovery and behavior training. The food restriction, 4-day pre-training (magazine and FR1 training),
474 7-day FR1 training, and 7-day NTC-FR4 training were the same as described earlier. The progressive
475 TC-FR4 training schedule followed the same criteria as described above. During the food restriction
476 and 4-day pre-training periods, saline (10mL/kg) was injected in the hM4Di and control groups. From
477 the first day of the FR1 training, all mice got i.p. clozapine-N-oxide (CNO) (Tocris,#6329, 5mg/kg
478 10mL/kg) injection before daily training sessions until the last day of the TC-FR4 training. The CNO
479 injection was performed 40-60 min before the operant task training and the mice stayed in their home
480 cages until each session started. The training chamber assignment and daily training order were
481 counterbalanced within each genotype. Male and Female mouse ratio was 5:5 within each

genotype. All mice underwent the same daily training protocol and received additional daily food supply (1-3g depending on the daily body weight) after the operant task training in their home cages.

Optogenetic Inhibition during sequence lever-press (TC-FR4) training

Within the SST-Cre-positive (Cre+) cagemates, individual mice were randomly assigned to either the eNpHR or eYFP groups, and AAV-DIO-eNpHR (or eYFP) was injected accordingly. As a result, all the mice in the eNpHR group had cage mates from the eYFP group, and they were housed together including during the period of surgical recovery and the entire behavioral training. The food restriction protocol started 2-3 weeks after the implantation surgery. Training protocols including food restriction, 4-day pre-training (magazine and FR1 training), 7-day FR1 training, and 7-day NTC-FR4 training remained consistent with previous descriptions. The 4-day pre-training was conducted under untethered conditions, while mice were tethered to optic fibers for one hour per day in their home cages. Starting from the first day of the 7-day FR1 training, all mice were tethered to optic fibers (Doric Lenses Inc, #SBP(2)_200/220/900-0.37_0.5m_FCM-2xMF1.25) and received closed-loop optogenetic inactivation during the operant training tasks. The laser illumination (Shanghai Laser, 532nm, 15mW at the cable tip with 200um core diameter) was turned on for 5 sec (continuous illumination) following every lever-press. The progressive TC-FR4 training schedule followed the same criteria as previously described. The eNpHR and eYFP groups were counterbalanced for daily training order and training chamber assignment. Both male and female mice were used with 5:5 ratio. All mice underwent the same daily training protocol and received additional daily food supply (1-3g depending on the daily body weight) after the operant task training in their home cages.

Definition of sequence (SEQ) efficiency

Sequence (SEQ) efficiency was developed as a mathematical expression for the simple description of structural features of efficient motor sequences. It is defined to describe the highest coefficient value when the structure and kinematics of motor sequences align with ideal patterns for a given task schedule, such as 4 lever-presses at 4Hz in the 4Hz-TC-FR4 schedule. Although mice could potentially receive rewards by executing more lever-presses at a faster rate during a sequence trial, such structures are inefficient due to wasted kinematics. From this optimal point, SEQ efficiency gradually decreases as the sequence contains an excessive or inadequate number of lever-presses or operates at an exceptionally high or low lever-press frequency. We implemented an equation for SEQ efficiency by employing a positively skewed gaussian distribution, denoted as ***S(x),*** which resulted in a 3-dimensional curve as a function of lever-press number ($\boldsymbol{x_{LEV}}$) and lever-press frequency ($\boldsymbol{x_{Hz}}$) within a sequence. The definition of SEQ efficiency is as follows:

$$SEQ\ efficiency(\boldsymbol{x_{LEV}}, \boldsymbol{x_{HZ}}) = 100\ \times\ S(\boldsymbol{x_{LEV}})\ \times S(\boldsymbol{x_{Hz}})$$

The skewed gaussian function ***S(x)*** is multiplication of a Gaussian function $\emptyset(x|\mu,\sigma)$ and a cumulative distribution function of the Gaussian distribution $\Phi(x|\mu,\alpha)$, and defined by the following formulas.

$$S(x) = 2\emptyset(x|\mu,\sigma) \times \Phi(x|\mu,\alpha)$$

$$\emptyset(x|\mu,\sigma) = \frac{1}{\sqrt{2\pi}}\exp\times\left(\frac{-(x-\mu)^2}{2\sigma^2}\right)$$

$$\Phi(x|\mu,\alpha) = \frac{1}{\sqrt{2\pi}}\int_{-\infty}^{\alpha(x-\mu)}\exp\left(\frac{-t^2}{2}\right)dt = \frac{1}{2}\left[1+\mathrm{erf}\left(\frac{\alpha(x-\mu)}{\sqrt{2}}\right)\right]$$

By adjusting coefficients (μ, σ, α), the asymmetric curvature of the skewed gaussian function is determined. We set $\mu = 2, \sigma = 4, \text{and } \alpha = 0.5$ to generate the mapping function shown in **Extended Figure 6**, where SEQ efficiency reaches its maximum value at Lever-press number/SEQ ($\boldsymbol{x_{LEV}}$) = 4 and lever-press frequency/SEQ ($\boldsymbol{x_{Hz}}$) = 4Hz. This mapping function empirically aligned with the behavioral data in TC-FR4 training (**Fig.2**), the modulation of sequence structures (**Fig.3**), and results in chemogenetic/optogenetic experiments (**Fig.4 and 5**).

Unsupervised hierarchical clustering for sequence (SEQ) classification

During TC-FR4 training, rewards were delivered by counting the most recent four consecutive lever-presses in real-time. If the total duration of these lever-presses fell within a specified time limit, the rewards were delivered immediately (delay less than 0.1sec). Timestamps for individual lever-presses, reward deliveries, and head entries were recorded in logfiles. In post-hoc analysis, sequence (SEQ) trials were defined as consecutive lever-presses followed by either a head entry or a pause longer than 3 seconds. For the SEQ clustering, each sequence was itemized and stored in a structured database, including key parameters such as lever-press/SEQ, frequency/SEQ, inter-sequence interval, reward success, optogenetic laser activation status, types of injected opsins, biological information (e.g., sex, age, genotype) of mice, acquired $\Delta F/F_0$ traces from calcium imaging, and the calculated SEQ efficiency. These itemized SEQ database, totaling 330 trials across 8 mice, were randomly shuffled before classification. In the unsupervised hierarchical clustering, only three structural kinematic parameters, lever-press/SEQ and frequency/SEQ, inter-sequence intervals, were initially used without considering any other sequence information, such as reward presentation or calculated SEQ efficiency. Once the classes of SEQ (e.g. C1,C2,and C3) were assigned by the clustering algorithm, the classification information was updated onto the itemized SEQ database. Then the data were reorganized depending on these classes (**Fig.3c,f, and g**). Reward-based classification (**Fig. 3h-p** and **Extended Fig.3**) was performed after the assignment of unsupervised classes. The hierarchical clustering and dendrogram analyses were conducted using a custom Python script (Python 3.10.6).

Brain slice electrophysiology recording

Mice were anesthetized with isoflurane and decapitated after deep anesthesia. The brain was rapidly harvested and transferred to a slicing chamber filled with ice-cold sucrose-based cutting solution containing the following (in mM): 194 sucrose, 30NaCl, 4.5 KCl, 26 $NaHCO_3$, 1.2 NaH_2PO_4, 10 D-glucose,1 $MgCl_2$, saturated with 95% O_2/5% CO_2. Coronal sections (250–300 μm) were collected using a Leica VT1200S Vibratome (Leica Microsystems, Buffalo Grove, IL, USA) and incubated in a chamber filled with artificial cerebrospinal fluid (aCSF) containing (in mM): 124 NaCl, 4.5 KCl, 26 $NaHCO_3$, 1.2 NaH_2PO_4,10 D-glucose,1 $MgCl_2$ and 2 $CaCl_2$, saturated with 95% O_2/5% CO_2. Slices were incubated for 30–60 min at 32°C and then maintained at room temperature prior to recording.
For patch-clamp measurement, brain slices containing hM4Di-mCherry-expressing SST cells in M1 were transferred to an upright microscope (Scientifica, Uckfield, UK) and visualized using a LUMPlanFL N×40/0.80 NA water immersion objective (Olympus, Waltham, MA, USA). For fluorescence imaging, excitation light (wavelength: 509-551nm) was generated via X-Cite LED driver (Lumen dynamics) and a cy3 filter-cube set and delivered through the objective to identify hM4Di-mCherry-expressing SST cells. Current clamp recordings were performed using an intracellular solution containing the following (in mM): 140 mM K-Glu, 10mM HEPES, 0.1 mM $CaCl_2$, 2 mM $MgCl_2$, 1 mM EGTA, 2 mM ATP-Mg, 0.2 mM GTP-Na. Micropipettes were made from 1.5 mm OD/1.12 mm ID borosilicate glass with a filament (World Precision Instruments, Sarasota, FL, USA) and resistance was 2–4 MΩ. Recordings were performed using a Multiclamp 700B and a Digidata 1550B digitizer with a low-pass filter setting of 2-10 kHz and a sampling frequency of 10kHz. Data were analyzed using pClamp 10.6 software (Molecular

565 Devices). After entering the whole cell configuration, we waited for 10 minutes and measured the
566 baseline membrane potential. Aftwerwards, CNO (Tocris #6329, 10μM) dissolved in aCSF was
567 continuously bath applied for at least 10 min.

568 **Histology**

569 After behavioral training and assessment, the mice were perfused with phosphate-buffered saline
570 (PBS) solution, followed by 4% paraformaldehyde. The brains were then extracted and postfixed in 4%
571 paraformaldehyde. After 24 hours of fixation, brains were transferred to PBS and stored at 4°C. For
572 sectioning, the posterior brain region from the superior colliculi was removed using a flat blade. Then,
573 the flat coronal cross-section of the brain was positioned and fixed on the flat vibratome stage using
574 superglue. 40μm (or 80μm)-thick sections containing M1 were prepared through the anterior to
575 posterior axis using a Leica VT1200S Vibratome (Leica Microsystems, Buffalo Grove, IL, USA). After
576 slice preparation, eNpHR-eYFP-expressing and GCaMP-expressing brain slices were mounted on
577 slides and covered with thin cover glasses after applying DAPI Fluoromount-G (Southern Biotech,
578 0100-20). The slices expressing hM4Di-mCherry or GCaMP6f were inspected under an epi-
579 fluorescence wide-field microscope (Zeiss AxioZoom.V16), and if necessary, additional
580 immunofluorescence staining was performed. First, the sections were washed four times for 20 minutes
581 each in PBS. Then, the sections were incubated in PBS containing 5% BSA and 0.2% Triton X in room
582 temperature. One hour later, the solution was replaced with a 0.5% BSA and 0.2% Triton X/PBS
583 solution (PBST) containing a 1:1,000 dilution of Rabbit anti-DsRed (Takara, #632496) or Chicken
584 Polyclonal anti-GFP antibody (Abcam, #ab13970), and the sections were incubated for 24 hours at
585 4°C. After the incubation in the primary solution, the sections were rinsed four times for 20 minutes
586 each with new PBST solution before incubation in a secondary antibody solution containing a 1:1,000
587 dilution of Goat anti Rabbit-AlexaFluor568 (Invitrogen, A-11011) or Goat anti-chicken AlexaFlour
588 488(Invitrogen, #A-11039) in PBST for 24 hours at 4°C. The sections were washed four times for 20
589 minutes in PBS before being mounted on slide glasses with DAPI Fluoromount-G (SouthernBiotech,
590 0100-20).

591

592 **Statistics**

593 For the data presentation illustrating neuronal responses (Fig. 1c, d, g, m, o, and Fig. 2g, h, k, q, s), we
594 averaged the trial responses of individual neurons to represent their characteristics. For all remaining
595 data presentations, we initially computed the mean of these neuronal responses to represent an
596 individual mouse and then calculated the averages across these individual mouse averages. The error
597 bars represent the standard error of the mean (s.e.m.) across mouse averages. All unpaired and
598 pairwise comparisons were two-tailed. Exact P values are reported in the figure captions. For analysis
599 of two experimental results (Fig.1q, Fig2 u) or two groups (Fig.4 b,c,d and Fig.5 b,c,d) across multiple
600 time periods, two-way repeated-measures ANOVA was used. For analysis of a single group across
601 variables (Fig 3 d,e,g), one-way repeated-measures ANOVA was used. When there were multiple
602 comparisons, the Sidak post hoc test was used when needed.

603

604

Acknowledgements

We would like to thank Drs. Karina Abrahao, Armando Salinas, Shana Augustin for advice on the project, technical support, and personal training. We also thank Drs. Joseph Cheer, Qing Liu, Kuan Hong Wang, Morgana Favero on technical support on head-mounted microscope systems, Dr. Andrew Kesner for help in use of the optogenetic laser controller, and Guoxiang Luo and Aurora Sheridan for tissue sample preparation. This work was supported by the Division of Intramural Clinical and Biological Research of the National Institute on Alcohol Abuse and Alcoholism (NIAAA).

Author Contributions

JOL, SB, and DML conceived and designed the study. JOL performed imaging, software programming, and behavior experiments with input from SB and DML. GS performed brain slice electrophysiology experiments with input from SB and DML. JOL, SB, GS, and DML analyzed data and wrote the manuscript. DML and SB directed the project.

Competing Interests

The authors declare no competing interests.

Data availability

Source data are provided with this paper. Raw data are available upon request to the corresponding author.

Code Availability

Custom codes used in this manuscript are deposited in the data base and publicly accessible at https://github.com/Jeongoenlee/SST.

REFERENCE

1. Xu, D., et al., *Cortical processing of flexible and context-dependent sensorimotor sequences.* Nature, 2022. **603**(7901): p. 464-469.
2. Graybiel, A.M., et al., *The basal ganglia and adaptive motor control.* Science, 1994. **265**(5180): p. 1826-1831.
3. Fee, M.S. and J.H. Goldberg, *A hypothesis for basal ganglia-dependent reinforcement learning in the songbird.* Neuroscience, 2011. **198**: p. 152-70.
4. Dhawale, A.K., M.A. Smith, and B.P. Olveczky, *The Role of Variability in Motor Learning.* Annu Rev Neurosci, 2017. **40**: p. 479-498.
5. Tumer, E.C. and M.S. Brainard, *Performance variability enables adaptive plasticity of 'crystallized'adult birdsong.* Nature 2007. **450**(7173): p. 1240-1244.
6. Wu, H.G., et al., *Temporal structure of motor variability is dynamically regulated and predicts motor learning ability.* Nat Neurosci, 2014. **17**(2): p. 312-21.
7. Zimnik, A.J. and M.M. Churchland, *Independent generation of sequence elements by motor cortex.* Nat Neurosci, 2021. **24**(3): p. 412-424.
8. Gilja, V., et al., *A high-performance neural prosthesis enabled by control algorithm design.* Nature neuroscience, 2012. **15**(12): p. 1752-1757.
9. Kupferschmidt, D.A., et al., *Parallel, but Dissociable, Processing in Discrete Corticostriatal Inputs Encodes Skill Learning.* Neuron, 2017. **96**(2): p. 476-489 e5.
10. Park, J., et al., *Motor cortical output for skilled forelimb movement is selectively distributed across projection neuron classes.* Sci Adv, 2022. **8**(10): p. eabj5167.
11. Masamizu, Y., et al., *Two distinct layer-specific dynamics of cortical ensembles during learning of a motor task.* Nat Neurosci, 2014. **17**(7): p. 987-94.
12. Hwang, E.J., et al., *Disengagement of motor cortex from movement control during long-term learning.* Sci Adv, 2019. **5**(10): p. eaay0001.
13. Dhawale, A.K., et al., *The basal ganglia control the detailed kinematics of learned motor skills.* Nature Neuroscience, 2021. **24**(9): p. 1256-1269.
14. Kawai, R., et al., *Motor cortex is required for learning but not for executing a motor skill.* Neuron, 2015. **86**(3): p. 800-12.
15. Jin, X. and R.M. Costa, *Start/stop signals emerge in nigrostriatal circuits during sequence learning.* Nature, 2010. **466**(7305): p. 457-62.
16. Peters, A.J., S.X. Chen, and T. Komiyama, *Emergence of reproducible spatiotemporal activity during motor learning.* Nature, 2014. **510**(7504): p. 263-7.
17. Huber, D., et al., *Multiple dynamic representations in the motor cortex during sensorimotor learning.* Nature, 2012. **484**(7395): p. 473-8.
18. Isomura, Y., et al., *Microcircuitry coordination of cortical motor information in self-initiation of voluntary movements.* Nat Neurosci, 2009. **12**(12): p. 1586-93.
19. Kaufman, M.T., M.M. Churchland, and K.V. Shenoy, *The roles of monkey M1 neuron classes in movement preparation and execution.* J Neurophysiol, 2013. **110**(4): p. 817-25.
20. Estebanez, L., et al., *Parvalbumin-Expressing GABAergic Neurons in Primary Motor Cortex Signal Reaching.* Cell Rep, 2017. **20**(2): p. 308-318.
21. Wang, X., et al., *Deconstruction of Corticospinal Circuits for Goal-Directed Motor Skills.* Cell, 2017. **171**(2): p. 440-455 e14.
22. Lee, C., et al., *Cell-type-specific responses to associative learning in the primary motor cortex.* Elife, 2022. **11**.
23. Churchland, M.M., et al., *Neural population dynamics during reaching.* Nature, 2012. **487**(7405): p. 51-56.

686 24. Tremblay, R., S. Lee, and B. Rudy, *GABAergic Interneurons in the Neocortex: From Cellular Properties to Circuits.*
687 Neuron, 2016. **91**(2): p. 260-92.
688 25. Petersen, C.C. and S. Crochet, *Synaptic computation and sensory processing in neocortical layer 2/3.* Neuron,
689 2013. **78**(1): p. 28-48.
690 26. Lee, S., et al., *A disinhibitory circuit mediates motor integration in the somatosensory cortex.* Nat Neurosci, 2013.
691 **16**(11): p. 1662-70.
692 27. Adler, A., et al., *Somatostatin-Expressing Interneurons Enable and Maintain Learning-Dependent Sequential*
693 *Activation of Pyramidal Neurons.* Neuron, 2019. **102**(1): p. 202-216 e7.
694 28. Cichon, J. and W.B. Gan, *Branch-specific dendritic Ca(2+) spikes cause persistent synaptic plasticity.* Nature,
695 2015. **520**(7546): p. 180-5.
696 29. Chen, S.X., et al., *Subtype-specific plasticity of inhibitory circuits in motor cortex during motor learning.* Nat
697 Neurosci, 2015. **18**(8): p. 1109-15.
698 30. Hattori, R., et al., *Functions and dysfunctions of neocortical inhibitory neuron subtypes.* Nat Neurosci, 2017.
699 **20**(9): p. 1199-1208.
700 31. Jin, X., F. Tecuapetla, and R.M. Costa, *Basal ganglia subcircuits distinctively encode the parsing and*
701 *concatenation of action sequences.* Nature Neuroscience, 2014. **17**(3): p. 423-430.
702 32. Sauerbrei, B.A., et al., *Cortical pattern generation during dexterous movement is input-driven.* Nature, 2020.
703 **577**(7790): p. 386-391.
704 33. Jiang, W., F. Tremblay, and C.E. Chapman, *Context-dependent tactile texture-sensitivity in monkey M1 and S1*
705 *cortex.* J Neurophysiol, 2018. **120**(5): p. 2334-2350.
706 34. Ferezou, I., et al., *Spatiotemporal dynamics of cortical sensorimotor integration in behaving mice.* Neuron, 2007.
707 **56**(5): p. 907-23.
708 35. Gentet, L.J., et al., *Unique functional properties of somatostatin-expressing GABAergic neurons in mouse barrel*
709 *cortex.* Nat Neurosci, 2012. **15**(4): p. 607-12.
710 36. Fujii, N. and A.M. Graybiel, *Representation of action sequence boundaries by macaque prefrontal cortical*
711 *neurons.* Science, 2003. **301**(5637): p. 1246-1249.
712 37. McColgan, P., et al., *The human motor cortex microcircuit: insights for neurodegenerative disease.* Nat Rev
713 Neurosci, 2020. **21**(8): p. 401-415.
714 38. Chen, K., et al., *Activation of cortical somatostatin interneurons rescues synapse loss and motor deficits after*
715 *acute MPTP infusion.* Iscience, 2019. **17**: p. 230-241.
716 39. Tennant, K.A., et al., *The organization of the forelimb representation of the C57BL/6 mouse motor cortex as*
717 *defined by intracortical microstimulation and cytoarchitecture.* Cereb Cortex, 2011. **21**(4): p. 865-76.
718 40. Zhou, P., et al., *Efficient and accurate extraction of in vivo calcium signals from microendoscopic video data.*
719 Elife, 2018. **7**.

720

721

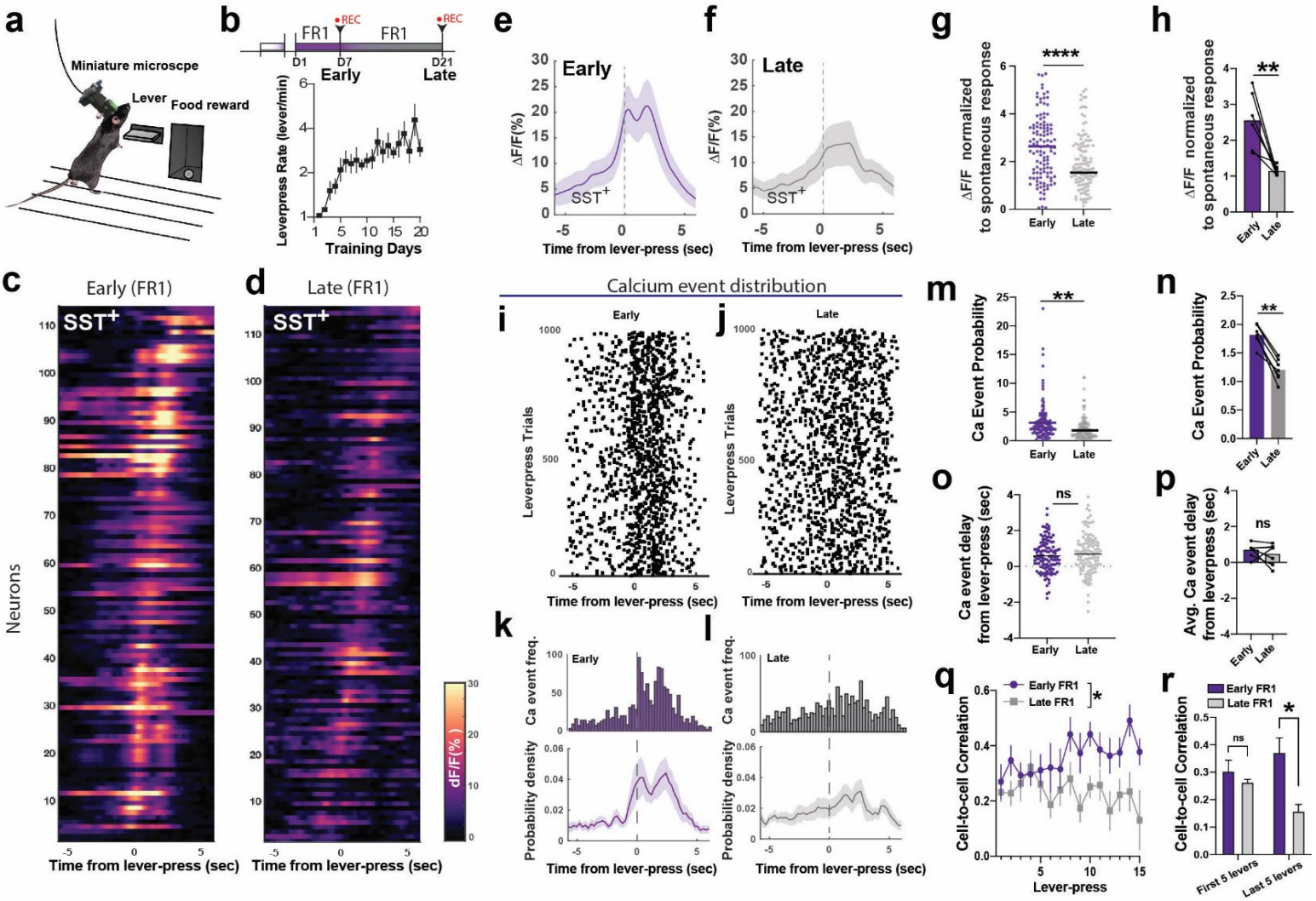

Figure 1. Action-specific activation of M1 SST network activity correlate with action acquisition and consolidation

(a) schematic of operant behavior training and in-vivo calcium activity imaging

(b) FR1 training schedule and the lever-press frequency, the lever-press kinematic was stabilized from D7 to D21. (n=7 mice)

(c) fluorescence calcium activity traces ($\Delta F/F_0$) of SST interneurons that are time-locked to the lever press on FR1 schedule D7 (n=117 cells) and (d) the same profile on D21 (n=119 cells)

(e) averaged $\Delta F/F_0$ (%, F_0 is spontaneous baseline) of SST interneurons time-locked to the lever press in early training (D7)

(f) averaged $\Delta F/F_0$ (%, F_0 is spontaneous baseline) of SST interneurons time-locked to the lever press in late training (D21)

(g) action-specific $\Delta F/F_0$ peak of individual SST+ interneurons, comparison between early (D7, n=117 cells) and late (D21, n=119 cells) training (two-tailed unpaired t-test, Mann-Whitney, ****p=0.0001), The peak $\Delta F/F_0$ is time-locked to the lever-press and normalized to spontaneous $\Delta F/F_0$ peak response

(h) the same action-specific $\Delta F/F_0$ peak in each animal, spontaneous $\Delta F/F_0$ peak response, comparison between early (D7) and late (D21) training (n=7mice, two-tailed paired t-test, p= 0.0036)

(i,j) calcium event distribution in D7 and D21 time-locked to the lever press, each dot denotes the retrieved peak location of $\Delta F/F_0$ traces, 1000 lever-press trials with corresponding calcium traces are randomly selected and shuffled (n=7 mice)

(k) accumulated distribution of calcium event frequency in (i) and averaged probability density function (bottom panel, n=7 mice) in D7

(l) accumulated distribution of calcium event frequency in (j) and averaged probability density function (bottom panel, n=7 mice) in D21

(m,n) action-specific calcium event probability in individual SST+ interneurons (each dots denote cells, n=117 cells in D7, n=119 cells in D21, two-tailed unpaired t-test, Mann-Whitney, p<0.0001) and animals (each dots denote animals, n=7 mice, two-tailed paired t-test, p= 0.0001), normalized to the average calcium event probability in spontaneous activity.

(o,p) average time delay of calcium event from the leverpress onset in individual cells is not significantly different (each dots denote cells, n=117 cells in D7, n=119 cells in D21,two-tailed unpaired t-test, p=0.3684) and animals (each dots denote animals, n=7 mice, two-tailed paired t-test, p=0.3864)

(q) correlation coefficients of action-specific SST calcium activity across lever-press trials were higher in early D7 training, while decreased in late D21 training. (two-way ANOVA, mixed-effects model, D7 early vs D21 late effect, p=0.0466, F(1,6)=6.244)

(r) correlation coefficient comparison between the first 5 levers and last 5 levers in early (D7) and late (D21) training sessions. In D21, the correlation coefficients of SST network activity are significantly lower on the last 5 lever-press in D7 early training compared to those in D21 late training (two-way ANOVA, repeated measure, D7 early vs D21 late effect, p=0.022, Sidak multiple comparison, last 5 levers of D7 early vs D21 late, p=0.0332). In all plots, shaded area and error bars denote SEM.

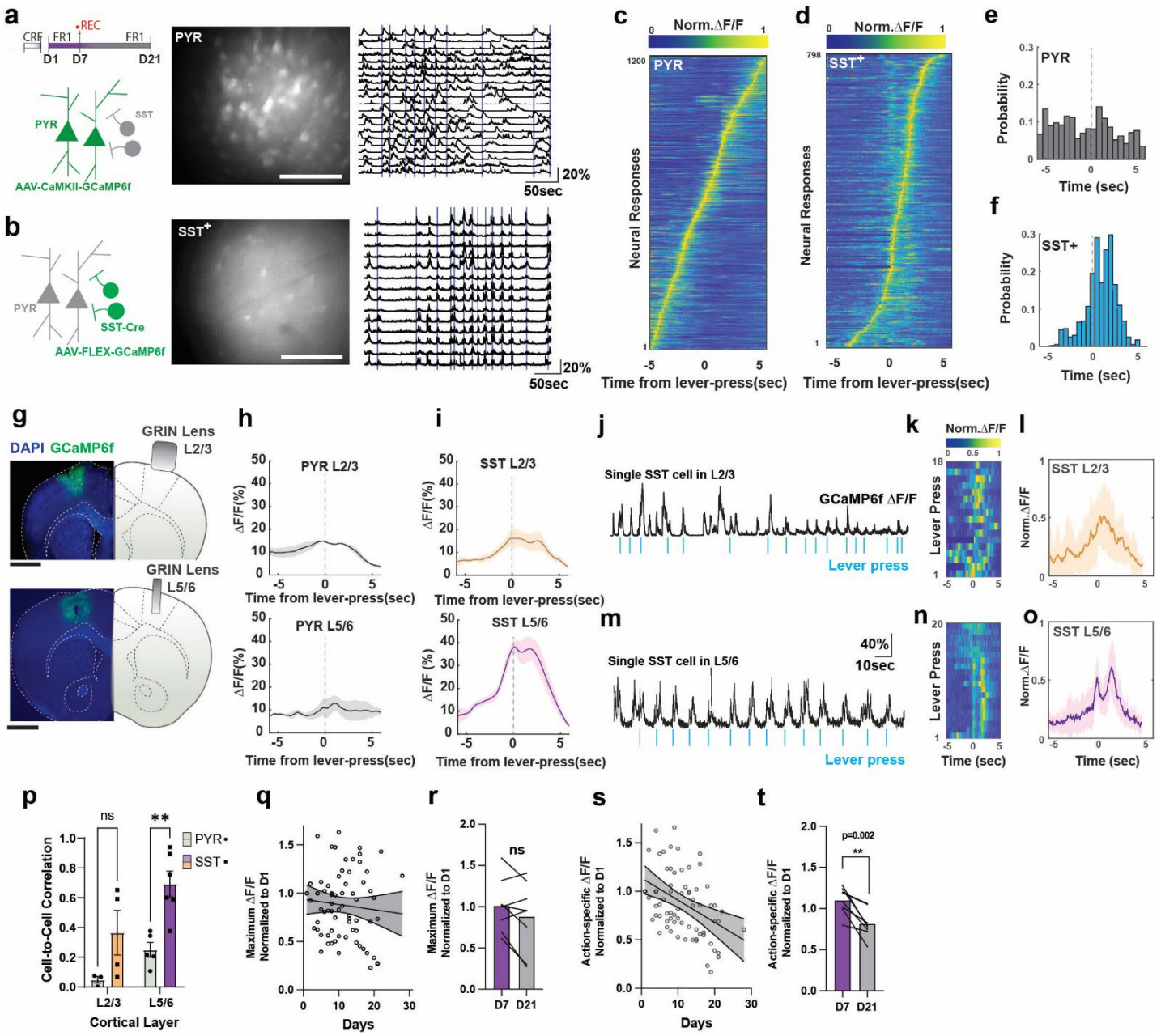

Extended Figure1. Single-cell and population activity of SST INs in M1 layer 5/6 display action-specific calcium response

(a) Raw fluorescence image of CaMKII driven GCaMP6f expression in M1 PYR neurons (left and mid panels). Scalebars in fluorescence images denote 100µm. Black traces in the right panel indicate de-synchronized $\Delta F/F_0$ calcium activity associated with lever-press events (vertical blue lines) **(b)** Raw fluorescence image of cre-dependent GCaMP6f expression in M1 SST(+) interneurons (left and mid panels) and synchronized calcium activity. **(c)** Peak normalized $\Delta F/F_0$ activity map of M1 PYR neurons displays sequential activation pattern around the leverpress onset. **(d)** Peak normalized $\Delta F/F_0$ activity map of SST(+) interneurons displays a temporally confined activation around the lever-press onset. **(e)** Calcium event probability distribution of PYR neurons, and **(f)** the same for SST(+) interneurons around the lever-press onset

(g) 1mm and 0.6mm GRIN lens were implanted in layer 2/3 and layer 5 respectively. Scalebar: 1.0mm **(h)** Population average of $\Delta F/F_0$ response in PYR neurons in L2/3 (483 neurons, n=3 mice) and L5 (347 neurons, n=4 mice) during lever-press **(i)** Population average of $\Delta F/F_0$ response in SST INs (L2/3, 117 neurons, n=4 mice) and (L5/6, 103 neurons, n=8 mice) during lever-press **(j)** Example of single cell $\Delta F/F_0$ trace of M1 SST interneuron in L2/3 **(k)** Peak normalized $\Delta F/F_0$ activity map of single cell in (j) time relative to the lever-press onset

(l) Averaged of peak normalized $\Delta F/F_0$ activity map in (k), (m) Example of single cell $\Delta F/F_0$ trace of M1 SST interneuron in L5/6 **(n)** Peak normalized $\Delta F/F_0$ activity map of single cell in (m) time relative to the lever-press onset **(o)** Averaged of peak normalized $\Delta F/F_0$ activity map in (n). **(p)** Cell-to-cell correlation coefficient of $\Delta F/F_0$ within a subject, each dot denotes an animal measurement in D7 (Two-way ANOVA, main effect: L2/3 vs L5/6, *p=0.0157 and PYR vs SST, **p=0.0015, Sidak post-hoc test: L5 PYR vs L5 SST, **p=0.0047) **(q)** Maximum $\Delta F/F_0$ response of L5/6 SST normalized to Day1 measurement. Fluorescence degradation was not significant (linear regression R^2=0.0095, slope non-zero p=0.7038) indicating consistent imaging measurement over 21 days. Each dot indicates max $\Delta F/F_0$ of one training session, and **(r)** comparison of the maximum $\Delta F/F_0$ ratio between D7 and D21 (n=8 mice, two-tailed paired t-test, p =0.1276) **(s)** Action-locked $\Delta F/F_0$ response of L5/6 SST normalized to Day1 measurement. Response degradation was significant (linear regression R^2=0.1595, slope non-zero p=0.0004). Each dot indicates average $\Delta F/F_0$ time-locked to lever-press within a training session, and (t) Action-locked $\Delta F/F_0$ ratio significantly decreased from D7 to D21 (n=8 mice, two-tailed paired t-test, p =0.0020). In all plots, shaded area and error bars denote SEM.

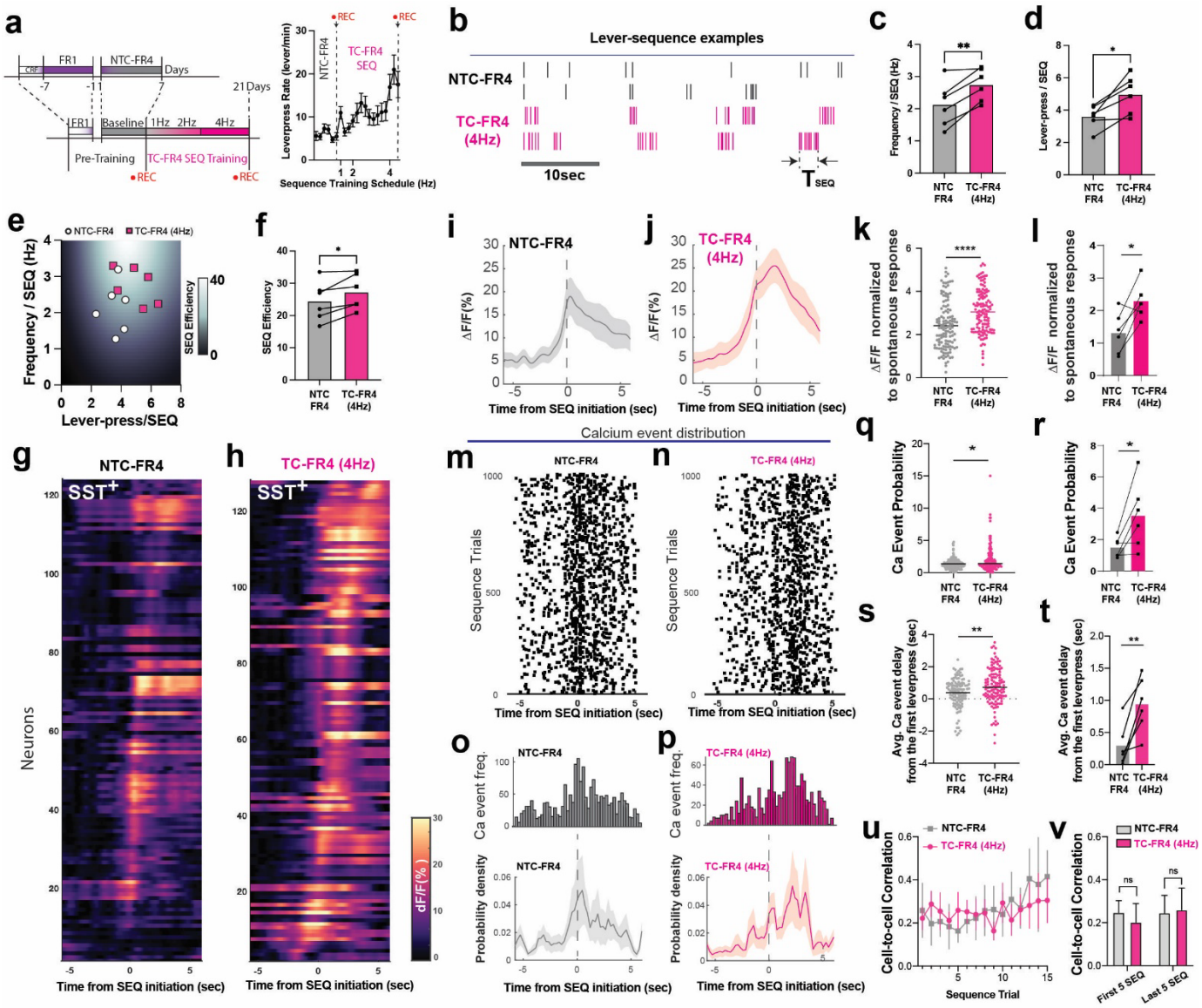

Figure 2. M1 SST interneurons increase calcium activity during execution of complex sequence

(a) Time-constrained FR4 (TC-FR4) sequence lever-press training schedule led mice to progressively increase lever-press rate in a session. Non-time-constrained criteria were assigned between D1 and D7 for FR4 schedule (NTC-FR4). From D8 to D21, mice had to press 4 consecutive leverpress within 4 sec (1Hz), 2sec (2Hz), 1sec (4Hz). **(b)** Example leverpress patterns are displayed as black bars (NTC-FR4 schedule), and magenta bars (TC-FR4 schedule, 4Hz). **(c)** The lever-press frequency (Hz) of a unit sequence trial significantly increased (n=6 mice, two-tailed paired t-test, **p= 0.0050) from NTC-FR4 to 4Hz-TC-FR4 schedule. **(d)** The lever-press number within a unit sequence significantly increased (n=6 mice, two-tailed paired t-test, *p= 0.0126). **(e)** Leve-press number and frequency (Hz) are projected onto the sequence efficiency coefficient map. Higher coefficient indicates a structured and efficient lever-press sequence at the 4Hz schedule. **(f)** The sequence structure coefficients between the NTC-FR4 schedule and 4Hz-TC-FR4 schedule. (n= 6mice, two-tailed paired-t test, p= 0.0244) **(g)** Fluorescence calcium activity traces ($\Delta F/F_0$) of SST interneurons (n=126 cells), time-locked at the sequence initiation, during the NTC-FR4 schedule. F_0 is the spontaneous fluorescence baseline. **(h)** The same data (n=128 cells) from the 4Hz-TC-FR4 training. **(i)** Averaged $\Delta F/F_0$ (%, F_0 is spontaneous baseline) of SST interneurons time-locked to the sequence initiation in the NTC-FR4 training schedule.**(j)** Averaged $\Delta F/F_0$ (%, F_0 is spontaneous baseline) of SST interneurons time-locked to the sequence initiation in the 4Hz-TC-FR4 training schedule. **(k)** Action-specific $\Delta F/F_0$ peak of individual SST interneurons, normalized to the spontaneous $\Delta F/F_0$ peak response, comparison between the NTC-FR4 schedule (n=126 cells) and 4Hz-TC-FR4 SEQ schedule (n=128 cells, two-tailed unpaired t-test, p<0.0001)

(l) Action-specific $\Delta F/F_0$ peak in each animal, normalized to the spontaneous $\Delta F/F_0$ peak response, comparison between NTC-FR4 and 4Hz-TC-FR4 training (n=6 mice, two-tailed paired t-test, p= 0.0171) **(m,n)** Calcium event distribution in NTC-FR4 schedule and 4Hz-TC-FR4, each dot denotes the retrieved peak location from $\Delta F/F_0$ traces, 1000 lever-press trials were randomly selected (n=6 mice). **(o)** Accumulated distribution of calcium event frequency in (m) and corresponding averaged probability density function. **(p)** Accumulated distribution of calcium event frequency in (n) and corresponding averaged probability density function **(q,r)** Action-specific calcium event probability in individual SST+ interneurons (each dot in panel m, two-tailed unpaired t-test, Mann-Whitney p= 0.0170) and animals (each dot in panel n, two-tailed paired t-test, p=0.0348), normalized to the average calcium event probability in spontaneous activity. **(s)** Average time delay of calcium event from the lever-press sequence onset in individual cells during NTC-FR4 schedule (n=113cells) and 4Hz-TC-FR4 schedule (n=120 cells, two-tailed unpaired t-test, Mann-Whitney p= 0.0101) **(t)** The same time delay of calcium event from animal average (n=6 mice, two-tailed paired-t test, p=0.0071). **(u)** Correlation coefficient across leverpress trials and training periods was not significantly different (Two-way ANOVA mixed-model, sequence trial effect p=0.5448, training schedule effect, p=0.7550) between NTC-FR4 schedule and 4Hz-TC-FR4 schedule. **(v)** Correlation coefficient between the training schedules was not significantly different in the animal average (two-way ANOVA repeated measures, sequence trial effect p=0.3696, training schedule effect, p=0.7077). In all plots, shaded area and error bars denote SEM.

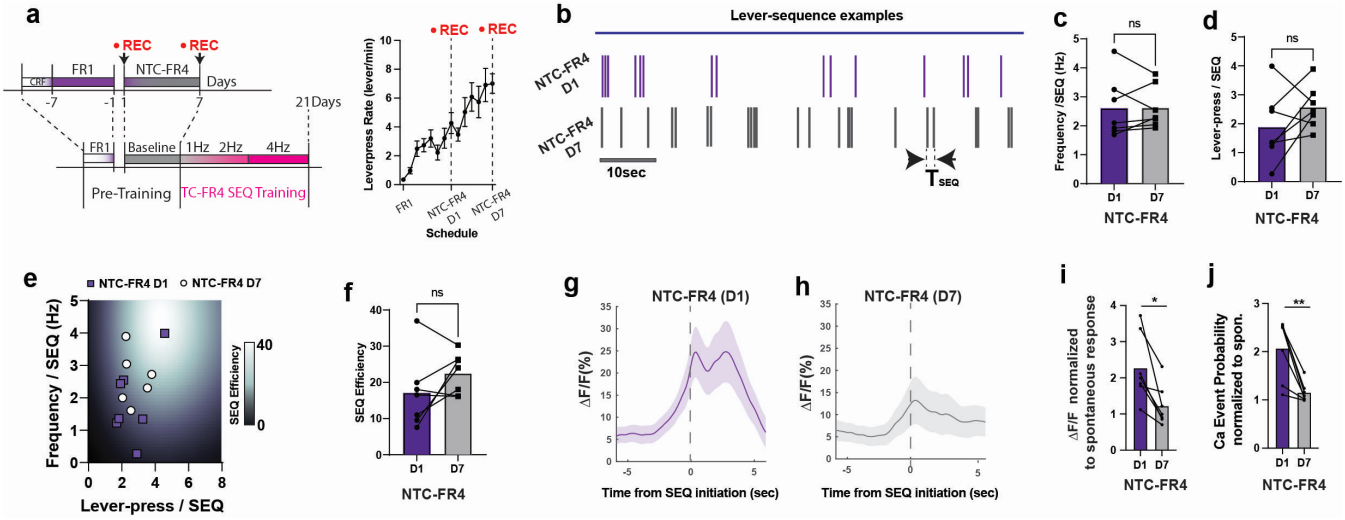

Extended Figure2. M1 SST activity was stabilized while the similar motor sequence structure was maintained.

(a) Pre-training schedule including FR1 and non-time-constrained FR4 training, before starting time-constrained sequence lever-press training. Average lever-press frequency per session (lever/min) increased as expected. In this static training schedule, consecutive lever-press and time-limit were not assessed for the reward delivery.

(b) Example lever-press patterns on the first day (D1, upper panel) and the seventh day (D7, lower panel) of non-time-constrained FR4 training.

(c,d) lever-press frequency and lever-press number per a unit sequence trial were not significantly altered for the 7 days of non-time-constrained FR4 training (n= 7mice, two-tailed paired t-test, p=0.9524, p= 0.1852), despite the increase in overall leverpress rate. Thus, the action kinematics of the action sequence was maintained.

(e) Leve-press number and frequency (Hz) are projected onto the sequence efficiency coefficient map in D1 (circle) and D7(square) of non-time-constrained FR4 training.

(f) The sequence efficiency coefficients between the D1 and D7 were not altered. (n= 7 mice, two-tailed paired t-test, p=0.1680).

(g) averaged $\Delta F/F_0$ (%, F_0 is spontaneous baseline) of SST interneurons in the non-time-constrained FR4 training schedule(D1), and **(h)** for D7.

(i) action-specific $\Delta F/F_0$ peak in each animal, normalized to the spontaneous $\Delta F/F_0$ peak response, comparison between D1 and D7 (n=7 mice, two-tailed paired t-test *p =0.010)

(j) action-specific $\Delta F/F_0$ peak in each animal, normalized to the spontaneous $\Delta F/F_0$ peak response, comparison between D1 and D7 (n= 7mice, two-tailed paired t-test, **p=0.0041). In all plots, shaded area and error bars denote SEM.

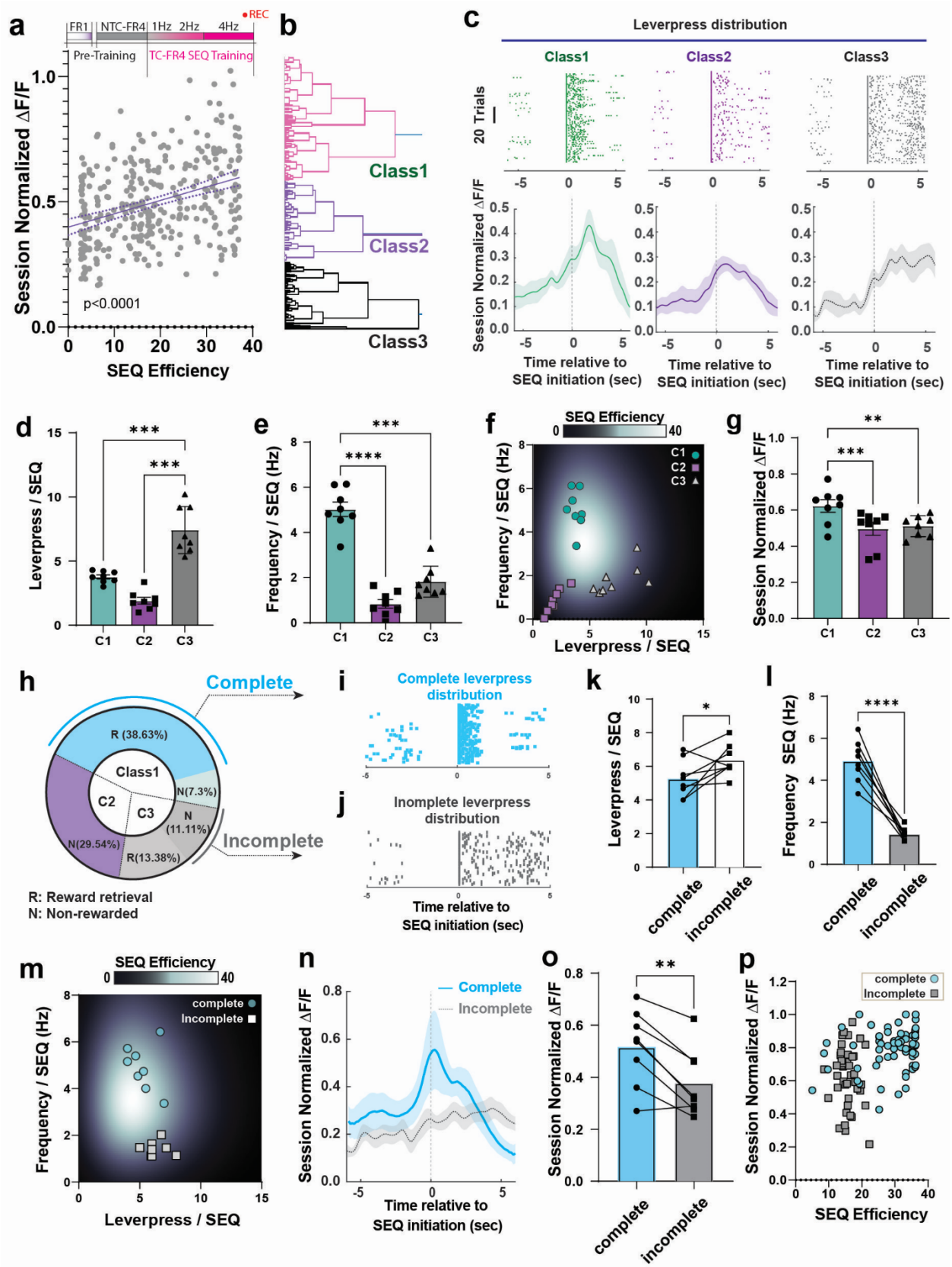

Figure3. Enhanced SST population activity correlates with kinematics and structure of motor sequences.
(a) Relationship between SEQ efficiency and peak $\Delta F/F_0$ of SST interneurons, normalized within a session and time-locked to the sequence initiation (each dot denotes sequence trials, total 330 SEQs, n=8 mice, linear regression R^2 =0.1331, slope deviation from zero p<0.0001)
(b) Unsupervised hierarchical clustering reveal three major classes (C1,C2, and C3) of lever-press sequences based on kinematic parameters

(c) Example lever-press distribution of classified sequence classes; (Class 1: fast and confined lever-press, n=62 SEQ trials), (Class 2: slow and temporally confined lever-press, n=37 SEQ trials), and (Class 3: slow and temporally elongated lever-press, n=127 SEQ trials) with corresponding fluorescence average of SST population activity $\Delta F/F_0$ (%, F_0 is spontaneous baseline).
(d) Lever-press number per sequence with respect to Class 1,2, and 3. (one-way ANOVA repeated measure, ***p<0.0001, Sidak multiple comparison test, C1 vs C3 ***p=0.0005 , C2 vs C3 ***p=0.0002)
(e) Lever-press frequency (Hz) per sequence with respect to Class 1,2, and 3. (one-way ANOVA repeated measure, ****p<0.0001, Sidak multiple comparison test, C1 vs C2 ****p<0.0001 , C1 vs C3 ***p=0.0001)
(f) Lever-press frequency (Hz) and lever-press number per sequence of C1, C2 and C3 are projected onto the sequence efficiency coefficient map, each dot denotes average coefficient of an animal (n= 8 mice)
(g) Maximum ΔF/F calcium responses of C1, C2, and C3, normalized within a session measurement and time-locked to the sequence initiation (One-way ANOVA repeated measure, ***p=0.0003, Sidak multiple comparison test, C1 vs C2 ***p=0.0002 , C1 vs C3 **p=0.035)
(h) Definition of complete (rewarded and temporally confined in C1) and incomplete (non-rewarded and temporally elongated in C3) sequences
(i) Example lever-press distribution of complete sequences and (j) incomplete sequences
(k) Lever-press number per sequence in complete and incomplete sequences (two tailed paired t-test, *p=0.0420)
(l) Lever-press frequency (Hz) per sequence in complete and incomplete sequences (two tailed paired t-test, ****p<0.0001)
(m) Complete and incomplete sequences projected onto a sequence efficiency coefficient map
(n) Fluorescence traces of SST population activity corresponding to complete and incomplete sequences, time-locked to the sequence initiation
(o) Maximum ΔF/F calcium responses (between 0-5 sec) of complete and incomplete sequences, time relative to the sequence initiation (two tailed paired t-test, **p=0.0037)
(p) Clustered distribution of complete and incomplete sequences in relation to SEQ efficiency coefficient and corresponding maximum ΔF/F normalized within a session (each dot denotes sequence trials). In all plots, shaded area and error bars denote SEM.

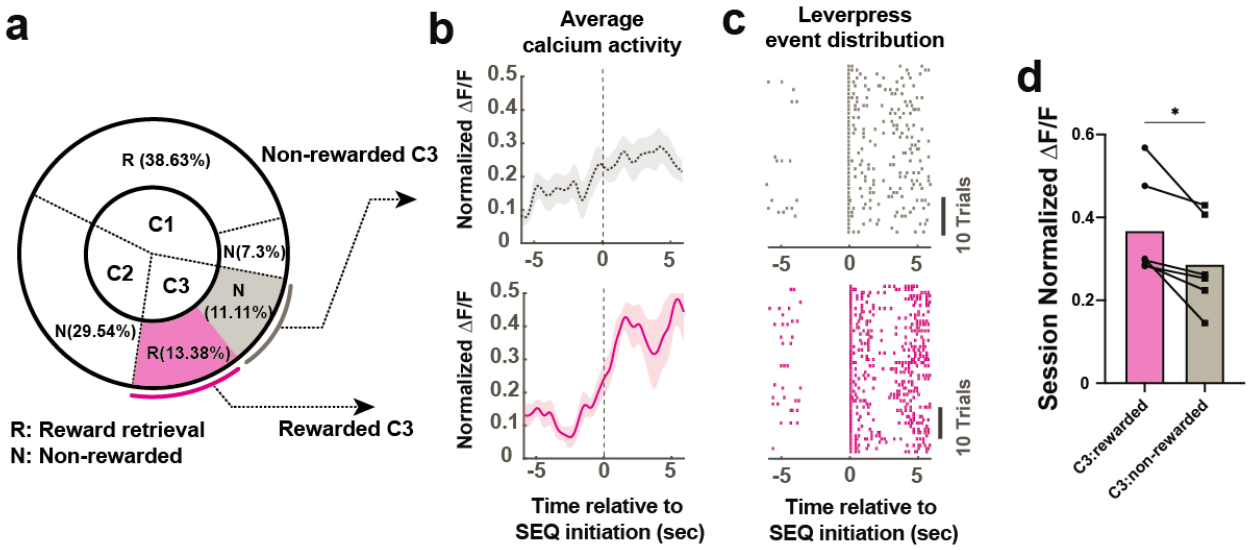

Extended Figure3. Sub-classes of rewarded and non-rewarded SEQs involve different SST-IN activity
(a) Rewarded and non-rewarded sequences within C3
(b) Average fluorescence traces of SST population activity corresponding to non-rewarded (upper) and rewarded sequences (bottom) within C3, normalized to session maximum and time-locked to the sequence initiation
(c) Example lever-press distribution of non-rewarded sequences (upper) and (j) the same for rewarded sequences (bottom) within C3
(d) Maximum ΔF/F calcium responses (between 0-5 sec) normalized within a session between C3 rewarded SEQ and C3 non-rewarded SEQs. (two-tailed paired sample Wilcoxon test *p=0.0313). In all plots, shaded area and error bars denote SEM.

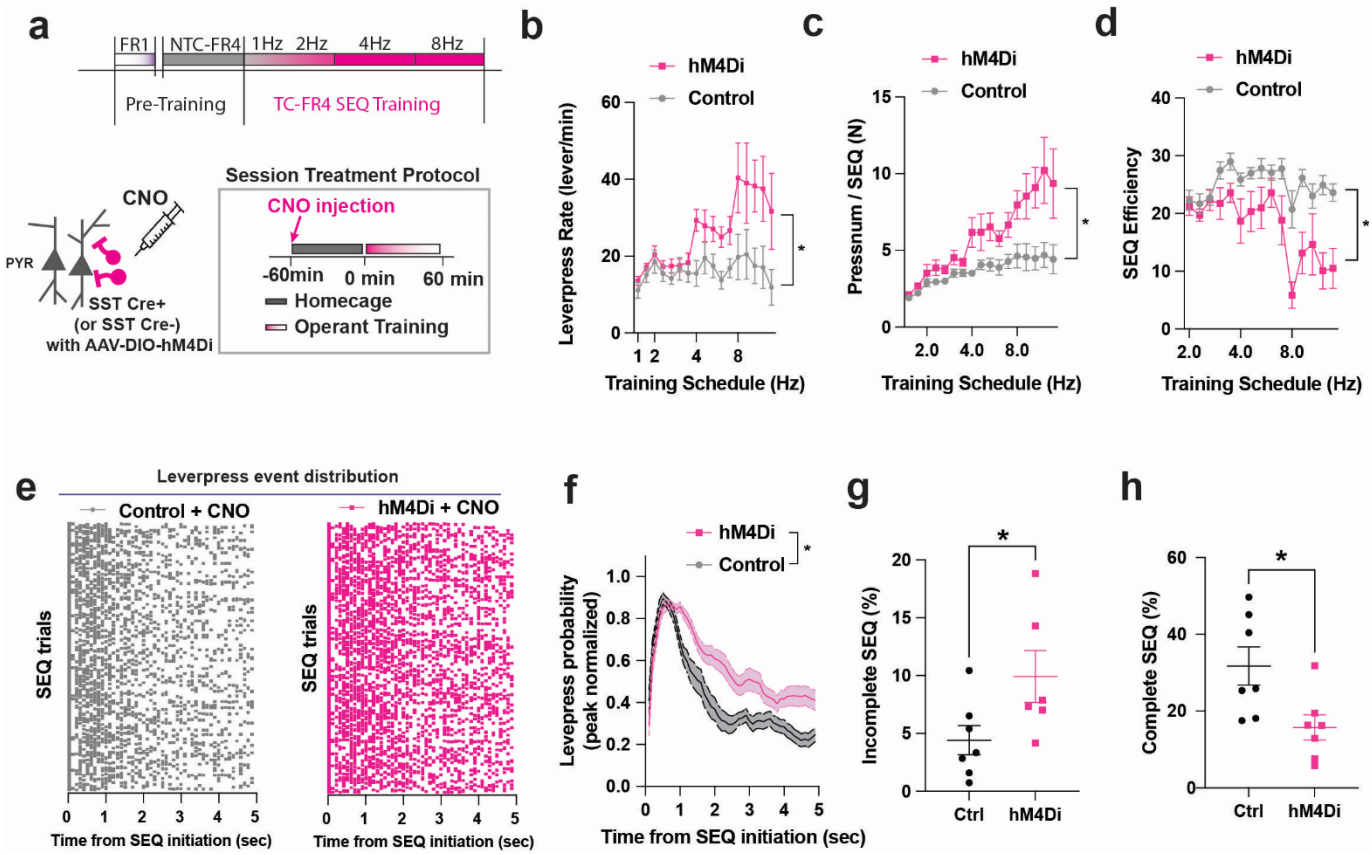

Figure 4. **Inhibition of SST interneurons disrupts kinematics of motor sequences.**

(a) Time-constrained FR4 sequence training schedule with hM4Di chemogenetic modulation

(b) Lever-press rate (levers/min) during a session increased in hM4Di-DREADD expressing mice (SST Cre-positive, n=6) and control mice (SST Cre-negative, n=7) with CNO injection (5mg/kg) on both groups (two-way ANOVA repeated measure. schedule ***p=0.0005, CNO treatment *p=0.0275, schedule x CNO ****p<0.0001)

(c) Number of lever presses per sequence increased in the hM4Di group, compared to the control group (two-way ANOVA repeated measure. schedule *p=0.0461, CNO treatment *p=0.03553, schedule x CNO *p=0.0165)

(d) Sequence efficiency coefficient (SEC) decreased in the hM4Di group compared to the control group (two-way ANOVA repeated measure. schedule ****p<0.0001, CNO treatment **p=0.0099, schedule x CNO ***p=0.0003)

(e) Representative lever-press event distribution in the control group (left, gray) and hM4Di group (right, magenta). Each dot denotes individual lever-press. Total 500 sequence (SEQ) trials were randomly selected from each group (control n=7 mice, hM4Di n=6 mice)

(f) Peak-normalized leverpress distribution probability. Time 0 is sequence initiation. The very first leverpress (SEQ initiation leverpress) was not included in the probability distribution. The hM4Di group shows elongated leverpress probability. (two-way ANOVA. Time ****p<0.0001, Group ***p=0.0001, Time x Group ****p<0.0001)

(g) Proportion (%) of incomplete sequence within in the total unrewarded trials increased in the hM4Di group compared to the control group (two-tailed unpaired t-test *p=0.0478). Each dot denotes average proportion of incomplete sequence per animal.

(h) Proportion (%) of complete sequence in the total rewarded SEQ trials decreased in the hM4Di group (two-tailed unpaired t-test *p=0.0197). In all plots, shaded area and error bars denote SEM.

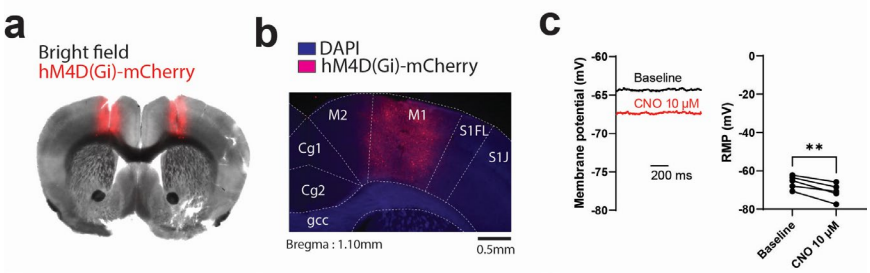

Extended Figure 4. hM4Di and CNO application alters resting membrane potential of SST interneurons in brain slices. (a) An example of a brain slice image used in electrophysiology experiments showing the expression of hM4Di-mCherry in M1 SST neurons. Slice thickness: 300µm. (b) Fluorescence image displaying hM4Di-mCherry expression in M1 SST neurons. (c) Effects of CNO (10µM) bath application on resting membrane potential (mV) measured in hM4Di-mCherry M1 SST neurons (N = 5 cells, 5 slices, 3 mice) (paired t-test, two-tailed, p** = 0.0036).

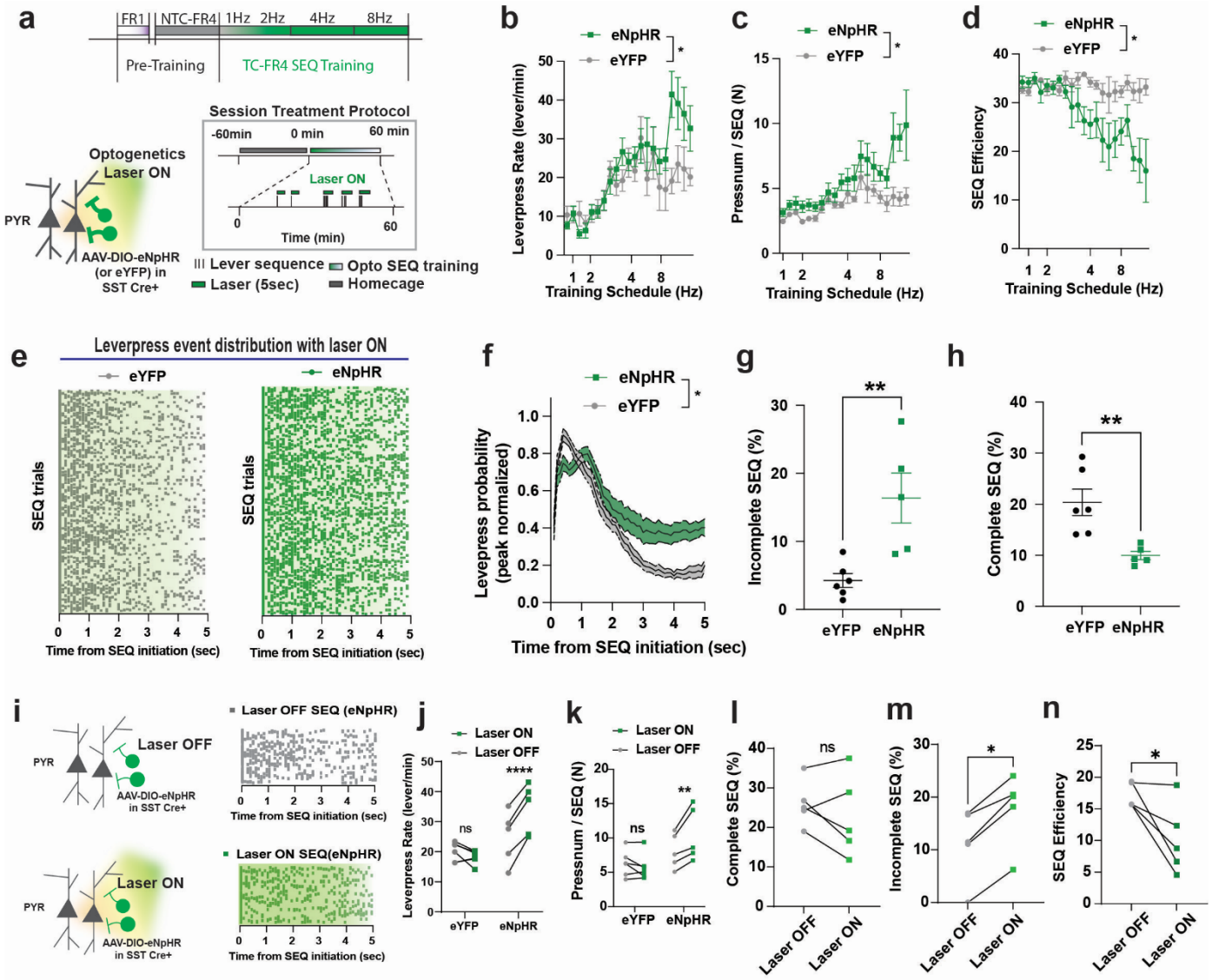

Figure 5. Action-specific inhibition of SST interneurons disrupts execution of efficient motor sequence.

(a) Time-constrained FR4 sequence training schedule and optogenetic modulation protocol. Each lever press triggers 5 sec of laser illumination (532 nm, ~4mW)

(b) Lever-press rate (levers/min) during a session increased in the eNpHR expressing mice (n=5), compared to the eYFP expressing control group (n=6) with the same opto-inhibition protocol. (two-way ANOVA repeated measure. Schedule ****p<0.0001, Treatment *p=0.0237, Schedule x Treatment ***p=0.0007)

(c) Number of lever presses per sequence increased in the eNpHR mice, compared to the eYFP mice (two-way ANOVA repeated measure. Schedule ****p<0.0001, Treatment *p=0.0293, Schedule x Treatment ***p=0.0002)

(d) Sequence efficiency coefficient (SEC) decreased in the eNpHR group compared to the eYFP group (two-way ANOVA repeated measure. Schedule **p=0.0024, Treatment *p=0.0114, Schedule x Treatment ****p<0.0001)

(f) Lever-press event distribution in the eYFP group (left, gray) and eNpHR group (right, green). Each dot denotes individual lever-press. Laser illumination is on during the 5 sec. Total 500 sequence (SEQ) trials were randomly selected from each group (eYFP n=6 mice, eNpHR n=5 mice).

(g) Peak-normalized lever-press distribution probability in eNpHR and eYFP mice. Time 0 is sequence initiation. The very first lever-press (SEQ initiation lever-press) was not included in the probability distribution curve. (two-way ANOVA. Time ****p<0.0001, Group **p=0.0078, Time x Group ****p<0.0001)

(h) Proportion (%) of incomplete sequence within in the total unrewarded trials increased in the eNpHR group compared to the control group (two-tailed unpaired t-test **p=0.0071). Each dot denotes average proportion of incomplete sequence per animal.

Proportion (%) of complete sequence in the total rewarded SEQ trials decreased in the eNpHR group (two-tailed unpaired t-test **p=0.0066).

(i) Lever-press event distribution in eNpHR mice during laser ON periods (upper panel) and OFF periods (lower panel) in periodic light modulation (PLM) protocol. Optogenetic laser illumination was alternatively enabled and disabled in every 5min.

(j) eNpHR group exhibited alteration in lever-press rate (levers/min) depending on the periodic laser modulation (5 min ON and 5 min OFF). Each dot represents an animal average (two-way ANOVA repeated measure, eYFP vs eNpHR effect: *p=0.0177, OFF vs ON effect: **p=0.001, Sidak multiple comparison within a group: OFF vs ON within eYFP p=0.1924, OFF vs ON within eNpHR ****p<0.0001)

(k) In the same training, only eNpHR group increased number of lever presses per sequence in the laser ON period than laser OFF period (Two-way ANOVA repeated measure, OFF vs ON effect: *p=0.0285, eYFP vs eNpHR effect p=0.0624, Sidak's multiple comparison test, laser on/off effect within eYFP p=0.5593, within eNpHR **p=0.0032)

(l) In the same PLM training schedule, proportion (%) of complete sequence was not significantly altered.

(m) Within the same eNpHR expressing subject, proportion (%) of incomplete sequence increased during laser ON periods compared to laser OFF periods (two-tailed unpaired t-test *p=0.0105). Each dot denotes average proportion (%) of incomplete sequence per animal.
(n) Sequence efficiency coefficient (SEC) decreased during laser ON periods compared to laser OFF periods (two-tailed Wilcoxon test *p=0.0312). In all plots, shaded area and error bars denote SEM.

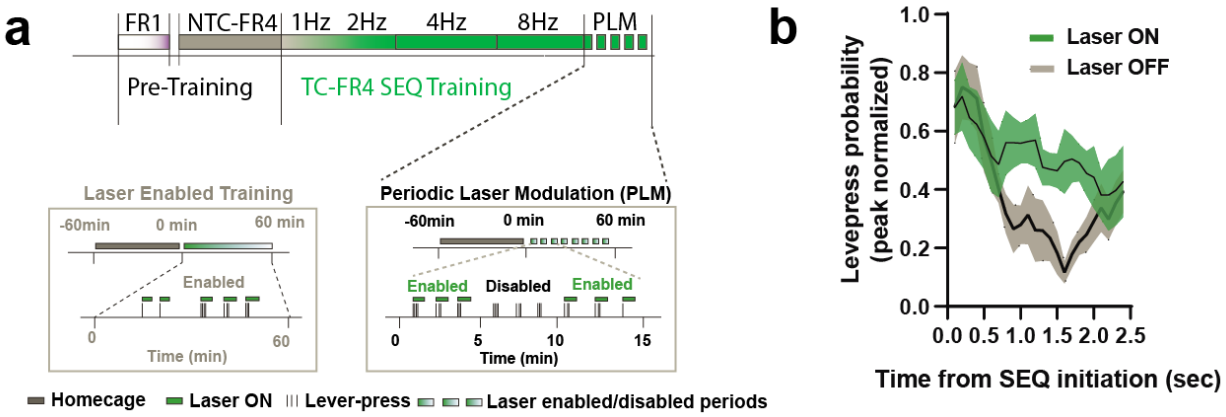

Extended Figure 5. Periodic Laser modulation (PLM) disrupts temporal structure of lever-press SEQs (a) PLM training schedule (b) lever-press distribution probability is elongated during the laser ON periods (green trace) compared to the laser OFF periods (gray trace). Time 0 is initiation of SEQs. Shaded areas indicate SEM.

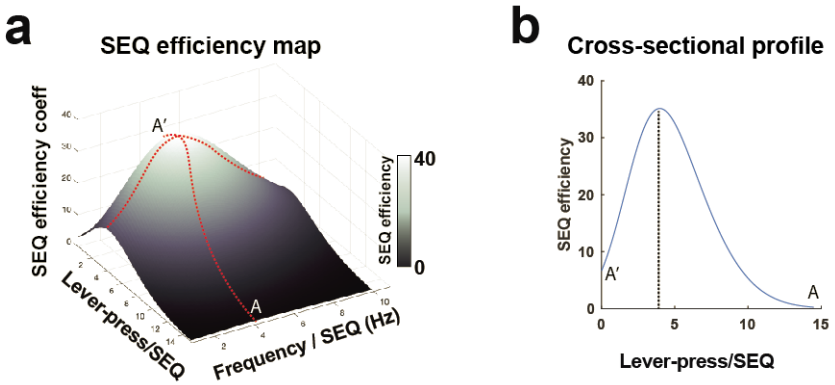

Extended Figure 6. SEQ efficiency map (a) A color-coded surface profile illustrating the SEQ efficiency map generated by skewed gaussian functions (b) A cross-sectional profile of the SEQ efficiency map along the red line, spanning from A-A′, with the frequency/SEQ set at 4Hz. The peak locations in the color-coded surface and the distribution curve indicate the most optimal structure of motor sequences with 4Hz and 4 lever-presses per SEQ.